Since January 2020 Elsevier has created a COVID-19 resource centre with free information in English and Mandarin on the novel coronavirus COVID-19. The COVID-19 resource centre is hosted on Elsevier Connect, the company's public news and information website.

Computers in Biology and Medicine 150 (2022) 106181

Contents lists available at ScienceDirect

Computers in Biology and Medicine

journal homepage: www.elsevier.com/locate/compbiomed

Research on multi-modal autonomous diagnosis algorithm of COVID-19 based on whale optimized support vector machine and improved D-S evidence fusion

Guowei Wang [a], Shuli Guo [a,*], Lina Han [b,*], Xiaowei Song [a], Yuanyuan Zhao [a]

[a] State Key Laboratory of Intelligent Control and Decision of Complex Systems, School of Automation, Beijing Institute of Technology, Beijing 100081, China
[b] Department of Cardiology, The Second Medical Center, National Clinical Research Center for Geriatric Diseases, Chinese PLA General Hospital, Beijing, China

ARTICLE INFO

Keywords:
COVID-19
Multi-modal information
Support vector machine
D-S evidence theory
Whale optimization algorithm

ABSTRACT

Aiming at the problem that the single CT image signal feature recognition method in the self-diagnosis of diseases cannot accurately and reliably classify COVID-19, and it is easily confused with suspected cases. The collected CT signals and experimental indexes are extracted to construct different feature vectors. The support vector machine is optimized by the improved whale algorithm for the preliminary diagnosis of COVID-19, and the basic probability distribution function of each evidence is calculated by the posterior probability modeling method. Then the similarity measure is introduced to optimize the basic probability distribution function. Finally, the multi-domain feature fusion prediction model is established by using the weighted D-S evidence theory. The experimental results show that the fusion of multi-domain feature information by whale optimized support vector machine and improved D-S evidence theory can effectively improve the accuracy and the precision of COVID-19 autonomous diagnosis. The method of replacing a single feature parameter with multi-modal indicators (CT, routine laboratory indexes, serum cytokines and chemokines) provides a more reliable signal source for the diagnosis model, which can effectively distinguish COVID-19 from the suspected cases.

1. Introduction

At present, COVID-19 epidemic is spreading rapidly all over the world, seriously endangering the human health and life, and it causes huge losses to people's lives and economy. COVID-19 is an infectious disease with strong infectivity and rapid transmission speed [1]. According to the statistics of the World Health Organization, the average number of infected people who will spread the virus to other people in the population without immunity is 3.77 [2]. Without medical intervention, the disease will spread rapidly. The current gold standard for diagnosing COVID-19 is RT-PCR performed on the respiratory tract collection [3]. However, it has the disadvantages of long time, complex process and low positive rate. In addition, it also has the problems of short supply of detection kits, insufficient detection capacity and wrong detection results, which may lead to the further spread of COVID-19. It is reported that almost all patients with COVID-19 may have lung changes during the course of the disease [4]. CT has the advantages of non-invasive, rapid and high sensitivity in the diagnosis of COVID-19, and it plays a vital role in the early detection of COVID-19, the identification of suspected cases and the evaluation of curative effect. The specific imaging features of COVID-19 include multiple small patch shadows and interstitial changes in the early stage, especially in the extrapulmonary zone. Further, it develops into multiple ground-glass opacity and infiltrating shadows in both lungs. In severe cases, the lung consolidation may occur and the pleural effusion is rare [5]. Although CT image is helpful for early screening of suspected cases, COVID-19 still has certain similarities with viral pneumonia and bacterial pneumonia in imaging manifestations, and it is difficult for doctors to identify COVID-19 with experience directly.

COVID-19 is diagnosed based on the comprehensive analysis of epidemiological history, clinical manifestations and experimental tests. Among them, the positive nucleic acid test is the primary standard for diagnosis [6]. Imaging combined with experimental tests for the diagnosis of COVID-19 is becoming more and more popular [7]. Although it brings dawn to the diagnosis and treatment of COVID-19, a large amount of data also brings a heavy burden to doctors. Therefore, the development of computer-aided diagnosis (CAD) will become a necessity [8]. As a new technology in the medical field, artificial intelligence has great advantages over the traditional methods that

* Corresponding authors.
E-mail addresses: guoshuli@bit.edu.cn (S. Guo), 2438381279@qq.com (L. Han).

https://doi.org/10.1016/j.compbiomed.2022.106181
Received 28 July 2022; Received in revised form 19 September 2022; Accepted 1 October 2022
Available online 5 October 2022

rely heavily on manual labor of lung lesions in CT images [9,10]. Gupta uses the improved random walk (IRF) algorithm to automatically segment the ground-glass opacity (GGO), combined with the gray level co-occurrence matrix, rotation-invariant uniform local binary pattern and Gabor filtering method to generate the feature vector. It uses the interactive information to reduce the dimension and adopts the improved random forest model to classify GGO [11]. Bayoudh used two methods of random translation and rotation of the image center coordinates to expand the positive samples, and the trained convolutional neural network 2D-CNN for GGO detection [12]. Zhang proposed the expansion layer instead of the convolution layer to increase the receptive domain and improve the ability of the network to learn the global information of the image. After improving the U-net network, the deep convolutional neural network (DCNN) model is formed [13]. Elaziz proposed a method for GGO segmentation and feature extraction by using multi-level threshold (MLT). GGO can be effectively detected by properly extracting the features of nodules. This algorithm mainly depends on the selection of the threshold, which has a great influence on the result. The change of the threshold means recalculation and the amount of calculation increases [14]. Nave proposed the plaque-based multi atlas method (PBMA). Through the feature vector based on size and shape, a group of minimum number of training samples are created, and each sample has the similar size and shape to the actual patient GGO image. The Laplace algorithm of Gaussian speckle detection method is used to find the segmentation region of GGO, which improves the detection sensitivity and solves the problem of high false positive rate [15]. Anter proposed a GGO detection algorithm using region growth and adaptive fuzzy C-means (AFCM) technology to reduce false positives in the nodule detection by clustering and then classifying [16]. Soui proposed a GGO detection algorithm based on AdaBoost cascade classifiers (ABC), which defined the GGO detection problem as the task of constructing classifiers, and it realized GGO detection in the form of classifiers to learn the mapping from original data to object classification [17]. In recent two years, some scholars have studied the methods of autonomous disease diagnosis and protection of medical data privacy. Hu [18] proposed the colorectal polyp region saliency detection method (CPRS) based on a variety of prior knowledge decisions. The rough saliency map is obtained based on the image background prior. In order to suppress the false detection of non-focus areas, the frequency prior and the adaptive center prior are incorporated to optimize saliency. The final fine saliency map is obtained by image cutting optimization to detect the colorectal polyp region in the ultrasound image. Wu [19] proposed an electronic medical record privacy protection algorithm based on the sensitive attribute clustering, which protects the privacy information of the data owner by deleting data and generalizing data. Such research methods only focus on the privacy of data, but it do not consider the accuracy of data. Zhou [20] proposed the graph-based extreme learning machine (GBELM) to solve the impact of discrete points and noise samples on EEG classification and improve the classification performance, but the ability to process the data needs to be improved. Yan [21] proposed an early classification method on time series, which reduces the dimension of time series samples, and then the samples are classified in low dimensional space. The proposed method is superior to the existing methods in accuracy and reliability. Dai [22] proposed the intelligent rehabilitation technology of EMG, which can effectively support quantitative diagnosis and rehabilitation efficacy evaluation, and it assists the rehabilitation robot to achieve safe and natural human–computer interaction. Tang [23] optimized the parameters of the BP neural network image segmentation method, and it further modified the training samples by extracting the image domain features. Using the improved BP neural network image segmentation method, the image is segmented from three aspects: the whole connected domain, the local domain and the edge domain. He [24] proposed an image segmentation algorithm based on neural network. The edge of image segmentation is clear, and the algorithm effectively shortens the time of sample training. Wu [25] proposed a location privacy protection method for private information retrieval. Based on the attribute encryption and the essential characteristics of location service, this method completes the location service query and feedback with zero information leakage through calculation between the user and the location server. Wu [26] proposed a searchable encryption method, which reduces the difficulty of key management in a multi-user environment, and the trap gate in the scheme can be transmitted on a non-secure channel with fine-grained access control, and the user's access rights can be increased or revoked according to the request of the data owner. Table 1 summarizes the names, references, advantages and limitations of related COVID-19 autonomous diagnosis algorithms. The autonomous diagnosis method for COVID-19 contains adjustable parameters, so the meta-heuristic algorithm can be used to optimize the adjustable parameters to achieve the best classification effect. Recent metaheuristics include monarch butterfly optimization (MBO), slime mould algorithm (SMA), moth search algorithm (MSA), hunger games search (HGS), Runge Kutta method (RUN), and Harris hawks optimization (HHO). Feng [27] proposed MBO based on reverse learning and random local disturbance, which improves the optimization efficiency of MBO. However, this method moves in a single way. It shares less information between populations and shows slower convergence. Li [28] proposed improved SMA, which uses adaptive weights to simulate the positive and negative feedback process of slime mold propagation waves based on biological vibrators to form an optimal path connecting food with good exploration ability. Wang [29] proposed the novelty MSA, which has the advantages of few parameters and strong robustness, which is rapidly applied to parameter extraction. However, the algorithm is prone to fall into local optimization in the later stage of iteration. Yang [30] proposed the HGS to build a prediction model and optimize the parameters through HGS. With the advantages of easy convergence, high convergence accuracy and escaping from the local optimal solution, it found a better global approximate optimal solution to obtain a model with higher classification accuracy. Ahmadianfar [31] proposed the RUN with variable step size strategy to achieve adaptive optimization control. The simulation results show that the predictive control algorithm has fast response speed, strong robustness and strong practicability. Houssein [32] proposed the improved Harris Hawks Optimization (IHHO) algorithm integrating mutualism. Tent chaotic map is used to initialize the population, which increases the diversity of population and improves the optimization performance of the algorithm. Table 2 summarizes the names, references, advantages and limitations of related meta heuristic algorithms. Although there are many diagnostic methods for COVID-19, they still do not meet the requirements for clinical application. There are also the following shortcomings: (1) The CT manifestations of patients with COVID-19 are different types of GGO, but GGO is not the specific imaging manifestation of COVID-19, which can appear in a variety of lung diseases [33,34]. It needs to be distinguished by combining blood routine, RT-PCR, cytokines and other experimental indexes; (2) The autonomous diagnosis of COVID-19 based on a single classifier has the shortcomings of low accuracy, strong randomness and poor robustness. The kernel parameter c and punishment parameter g of the SVM are mainly selected by experience, and the prediction accuracy cannot meet the actual needs; (3) The traditional method of the weighted evidence fusion is sensitive to the basic probability distribution function and it lacks robustness. In the face of high conflict evidence, there is a fusion failure problem, and the influence of the consistency of diagnosis results on the fusion results is not considered, which has certain defects.

Whale optimization algorithm (WOA) is a new optimization algorithm, which has the advantages of few parameters, simple operation, fast convergence speed and strong optimization ability. The MSVM model contains adjustable parameters, so the classification performance of MSVM can be improved by selecting different values. In this paper, WOA is used to optimize the adjustable parameters. The optimization of MSVM by WOA can accelerate the optimal speed of the adjustable

Table 1
Literature review of COVID-19 autonomous diagnosis algorithms.

Algorithm	Reference	Advantage	Limitation
IRF	Ref. [11]	It is good at processing high-dimensional data.	It is easy to overfit.
2D-CNN	Ref. [12]	Feature extraction can be performed automatically.	Parameter adjustment is required, and classification speed is slow.
DCNN	Ref. [13]	It has very good robustness and stability.	A large number of samples are required.
MLT	Ref. [14]	The calculation is small and the complexity is low.	Its classification accuracy is low.
PBMA	Ref. [15]	It has very good robustness.	The amount of calculation is large.
ABC	Ref. [17]	Different classification algorithms can be used as weak classifiers.	Training is time-consuming and it is easily affected by data distribution.
CPRS	Ref. [18]	The operation speed is fast.	Correlations of attributes in the dataset are ignored.
GBELM	Ref. [20]	It can solve nonlinear problems and it has strong generalization ability.	When the sample is unbalanced, the prediction deviation is relatively large.

Table 2
Literature review of meta heuristic algorithms.

Algorithm	Reference	Advantage	Limitation
MBO	Ref. [27]	Convergence accuracy is accelerated.	Time complexity is increased.
SMA	Ref. [28]	Population diversity is increased.	Speed of early convergence is slow
MSA	Ref. [29]	Convergence accuracy is accelerated.	Running time is increased.
HGS	Ref. [30]	Convergence is improved.	It is easy to fall into local optima.
RUN	Ref. [31]	Accuracy and robustness of the solution are improved.	The data of simulation experiment is single.
IHHO	Ref. [32]	Local search capability is increased.	The ability to jump out of local optimum is weak.

parameters, which shortens the running time and improves the accuracy of COVID-19 autonomous diagnosis. Based on the above reasons, this study proposes an autonomous diagnosis algorithm for COVID-19 based on whale-optimized MSVM and improved D-S evidence fusion. The contributions of this work can be summarized as the following: (I) this paper proposes 58-dimensional feature components such as CT image features, blood routine, RT-PCR and cytokines are extracted to jointly quantify COVID-19; (II) this paper proposes an autonomous diagnosis method for COVID-19 based on the least weighted whale optimization algorithm to optimize the mixed kernel support vector machine. The whale algorithm is improved by introducing nonlinear factors and adaptive weights, and then the improved algorithm is used to optimize the parameters of mixed kernel SVM, so as to improve the optimization accuracy and convergence speed, and it prevents WOA from falling into local optimum prematurely; (III) a method based on the angle cosine and Lance distance is proposed to effectively solve the high conflict evidence. The conflict evidence is identified by the cosine of the included angle. For the existing conflict evidence, the Lance distance between the evidences in the system identification framework is calculated. Then the reliability of the evidence is taken as the weight, and the weighted average on the evidence sources is performed. The D-S synthesis rule is applied to the processed evidence source to obtain the fusion result. The experimental results show that the model can improve the rationality of feature structure and the performance of classification to a certain extent, so as to improve the detection effect of COVID-19. The algorithm model of multi-modal autonomous diagnosis algorithm for COVID-19 is shown in Fig. 1.

2. Multi-modal feature extraction and quantification of COVID-19

2.1. Characteristic analysis and quantification of GGO

Image features are the most basic attributes used to describe image content, and selecting reasonable features is the key for accurate GGO detection [35,36]. The selection of features is not unique, and the medical images generated by different types of GGO have different features [37]. GGO features are influenced by the comprehensiveness of its description and the accuracy of its characterization [38]. A large amount of noise information will reduce the feature extraction accuracy of GGO and affect the final detection results [39]. Therefore, in order to comprehensively and accurately express the morphological structure and local characteristics of GGO based on the analysis of medical signs of GGO, this study qualitatively analyzed and characterized the lesions from two-dimensional and three-dimensional perspectives. Fig. 2 shows three different types of GGO and the ROI segmentation results including COVID-19, bacterial pneumonia, viral pneumonia.

This paper focuses on autonomous diagnosis of COVID-19 based on the multi-modal indicators, not feature extraction. The feature extraction methods in this paper are referred from Ref. [3,40,41]. This paper only lists the types of COVID-19 multi-modal diagnosis indicators. In order to objectively describe the CT image characteristics of COVID-19, the description and equations of Hu moment and gray level co-occurrence matrix (GLCM) are expressed in this paper.

The Hu moment of an image is a kind of image feature with translation, rotation and scale invariance. The digital image is a two-dimensional discrete signal. The pth order Hu moment m_p of $f(x,y)$ after discretizing can be expressed as:

$$m_p = \sum_{x=1}^{C}\sum_{y=1}^{R} x^p y^p f(x,y) \tag{1}$$

where $f(x,y)$ represents the pixel value of the image; C and R represent the column and row of the image respectively; p represents the order, $p = 0, 1, 2\cdots$.

The GLCM is a method to count the gray level distribution of an image. The essence of its description is to count the frequency of a pair gray levels in a certain position. The GLCM defines a pair of pixel points with gray levels i and j in image I, with the direction is θ, and the probability of simultaneous occurrence distance d is recorded as $p(i,j,d,\theta)$. The specific expressions of the probability when the interval of direction θ is 45° are shown in Eq. (2) to Eq. (5).

$$p(i,j,d,0^\circ) = \#\{[(k,l),(m,n)]|k-m=0, |l-n|=d\} \tag{2}$$

$$\begin{aligned} &p(i,j,d,45^\circ) = \#\{[(k,l),(m,n)]|(k-m=d, l-n=-d) \\ &or(k-m=-d, l-n=d)\} \end{aligned} \tag{3}$$

$$p(i,j,d,90^\circ) = \#\{[(k,l),(m,n)]||k-m|=d, l-n=0\} \tag{4}$$

$$\begin{aligned} &p(i,j,d,135^\circ) = \#\{[(k,l),(m,n)]|(k-m=-d, l-n=-d) \\ &or\ (k-m=d, l-n=d)\} \end{aligned} \tag{5}$$

where # represents the number of elements in the set, $I(k,l) = i$, $I(m,n) = j$.

2.1.1. Shape feature

The shape features are the most intuitive visual features. It can represent the main medical signs of GGO, such as round mass sign, lobulation sign, and hairpin sign from the geometry shape, edge roughness and topological structure [42]. The shape feature components extracted in this paper mainly include: perimeter, area, volume, circularity, rectangularity, extension length, Euler number, circumscribed spherical

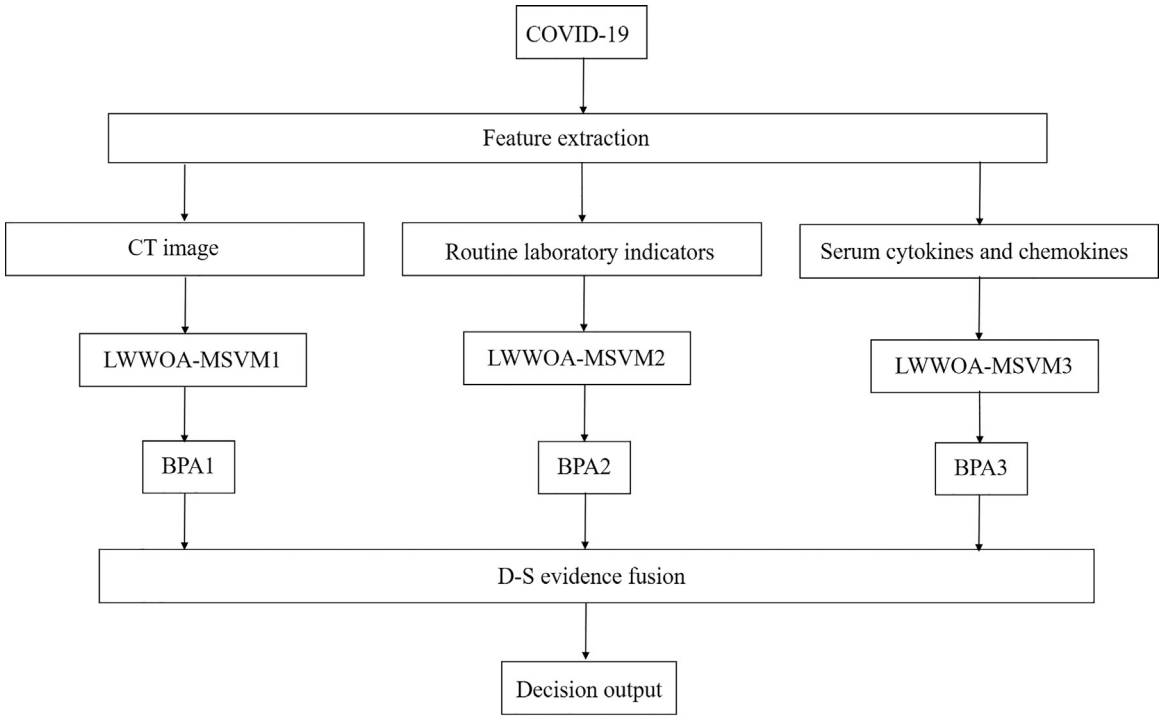

Fig. 1. Model of multi-modal autonomous diagnosis algorithm for COVID-19.

volume ratio, standard deviation of surface-center distance, number of corners, Hu moment, intersection distance of the circumscribed cuboid.

Circularity ($K = \frac{P^2}{4\pi A}$, A is the area of GGO, P is the perimeter of GGO) and rectangularity ($P = \frac{S}{R}$, S is the area of the connected domain, R is the minimum circumscribed rectangular area of the connected domain) are the main indicators to describe the geometric characteristics of GGO. The greater the value of both, the deeper the lobule, the more spinous processes, and the more irregular the shape.

Extension length ($N = \sum_{x,y} w(x,y)[I(x+u, y+v) - I(x,y)]^2$, $I(x,y)$ represents the gray value of the pixel, $w(x,y)$ represents the weight in the Gaussian window) can effectively describe the roughness of the GGO. The more corners, the rougher the edge, and the more leaves and spikes.

Number of Euler ($E_0 = C - H$, C is the number of connected regions and H is the number of cavities) can measure the cavitation characteristics of GGO. The smaller the number of cavities in the calculated region, the more holes are in GGO.

Circumscribed cuboid ($E_s(A_i) = \frac{Volume(A_i)}{Volume(VS(A_i))}$) is the ratio of each GGO extracted from CT images to the circumscribed sphere volume $VS(A_i)$, which reflects the similarity between the GGO and the sphere.

2.1.2. Intensity feature

The grayscale statistical feature is the most basic feature to describe the two-dimensional image area quantitatively, which is called the intensity feature from the three-dimensional perspective [38]. The intensity feature components extracted in this paper include intensity mean, intensity variance, maximum and minimum intensity difference, skewness, kurtosis, intensity gradient (from inside to outside) and Laplace divergence (mean, difference).

Intensity mean ($E(I) = \sum I * P(I)$, $P(I)$ is the pixel fractions of image I) reflects the overall brightness of the image, and intensity variance ($D(I) = E[(I - E(I))^2]$) reflects the contrast of the image. Because of the large brightness, strong contrast and rich information of the blood vessels. Therefore, when the size is similar, the mean value and variance of gray scale are also larger than those of GGO.

Skewness ($S(I) = \sum(I - E(I))^3 P(I)$) is the measurement of the asymmetric probability distribution of pixels, which is reflected in the degree of skew of the curve. Through observation, it can be found that most of the GGOs are the bright areas, which tend to be skewed distribution.

Kurtosis ($K(I) = \sum(I - E(I))^4 P(I)$) is the measurement of the sharpness of pixel probability distribution, which is reflected in the height of the peak of the distribution curve. The larger the kurtosis coefficient, the more extreme values of the distribution. The kurtosis coefficient of blood vessels is generally greater than GGO.

Intensity gradient ($G(x,y) = dx(i,j) + dy(i,j)$) reflects the changes on the gray scale of the edges of the image, which describes the edge differences between the GGO and other tissues.

The mean of Laplacian divergence ($E_{lm}(A_i) = mean(A_i \times La)$) is the result of convolution of Laplacian operator La and original CT image. According to the calculation results, it is found that the divergence of regions around GGO with small difference in gray values is obviously different. Therefore, calculating the average value of Laplacian divergence is helpful to distinguish GGO from interfering impurities.

The difference of Laplacian divergence ($E_{ld}(A_i = max(A_i \times La) - min(A_i \times La))$) is the difference between the maximum and minimum of the Laplacian divergence, which describes the variation range of the regional divergence.

2.1.3. Texture feature

This paper extracts the angular second-order moment, inertia moment, deficit moment, sum mean, variance, sum variance, difference variance, entropy, sum of entropy, difference entropy, information measure, correlation coefficient and maximum correlation coefficient based on GLCM. The roughness, contrast and orientation based on Tamura texture features are extracted.

The angular second-order moment ($ASM = \sum_i \sum_j p(i,j)^2$) is the measurement of the uniformity of gray distribution and texture thickness of the image. When the image texture is more detailed and the gray distribution is more regular, the smaller the ASM is; on the contrary, the more complex the image, the larger the ASM is.

Entropy ($Ent = -\sum_i \sum_j p(i,j) log p(i,j)$) is the measurement of the amount of texture information in an image. The more random the

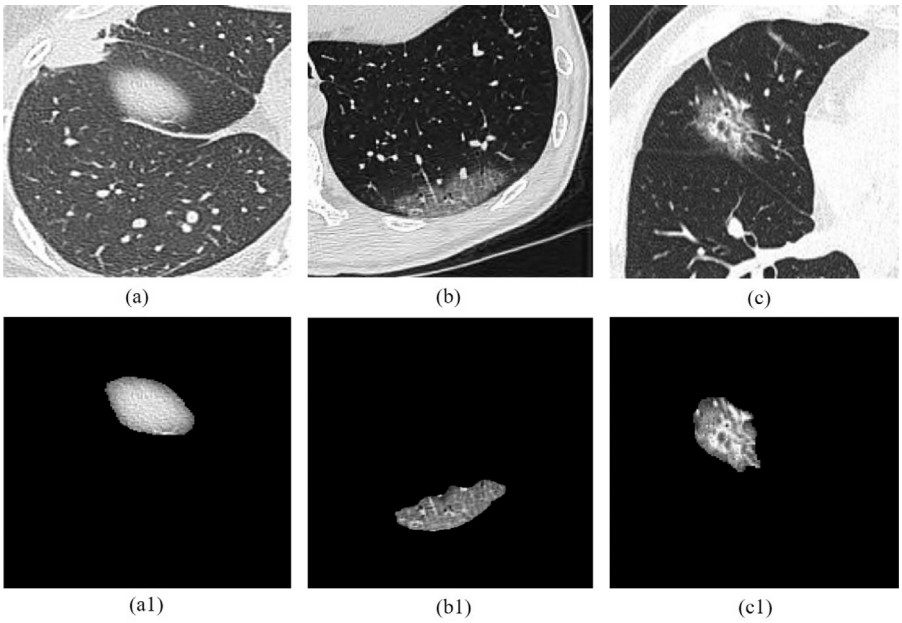

Fig. 2. Examples of the CT images in the disease advanced stage (a) COVID-19; (b) bacterial pneumonia; (c) viral pneumonia; (a1) ROI of COVID-19 segmented by doctor (gold standard); (b1) ROI of bacterial pneumonia segmented by doctor (gold standard); (c1) ROI of viral pneumonia segmented by doctor (gold standard).

gray value distribution of an image, the more approximately equal the array values in GLCM are, and the greater the entropy value is; on the contrary, the smaller the entropy, the smoother the image is.

Contrast ($con = \sum_i \sum_j (i-j)^2 p(i,j)$) measures how the texture values are distributed and the degree of local gray level changes in the image. The finer the image texture, the greater the contrast is, the clearer the image is, and the larger the Con. On the contrary, the rougher the texture, the smaller the Con is.

The inertia moment ($IDM = \sum_i \sum_j \frac{p(i,j)}{1+(i-j)^2}$) reflects the clarity and regularity of the texture. The clearer the texture, the more regular the gray distribution is, and the larger the IDM is.

Correlation coefficient ($corr = \frac{\sum_i \sum_j ((ij)p(i,j)) - \mu_x \mu_y}{\delta_x \delta_y}$) is used to measure the similarity of textures in row or column directions. Therefore, the size of the $Corr$ reflects the local gray correlation. The greater the texture correlation, the greater the $Corr$ is.

2.2. The test of routine laboratory indexes

The main CT performance of patients with COVID-19 is GGO. However, GGO is not specific imaging manifestations of COVID-19, and it can appear in a variety of lung diseases. It needs to be distinguished by other laboratory indicators such as blood routine and reverse transcription-polymerase chain reaction (RT-PCR). The blood routine indexes are detected by the blood cell analyzer, including white blood cell (WBC), lymphocyte (L), neutrophil (n) and hemoglobin (HB). The blood liver function, renal function, blood glucose, blood lipids and other related indicators are detected by the biochemical analyzer, including alanine aminotransferase (ALT), aspartate aminotransferase (AST), total bilirubin (T-Bil), glutamyl transferase (GGT), albumin (ALB), cholinester enzyme (ChE), alkaline phosphatase (ALP), lactate dehydrogenase (LDH), glucose (Glu), calcium (Ca2+), total cholesterol (TC), triglyceride (TG) and C-reactive protein (CRP). The coagulation function indexes are detected by the autonomous blood coagulation analyzer, including thrombin time (TT), prothrombin time (PT), fibrinogen (Fib), activated partial thrombin time (APTT) and D-dimer (D-Dimer). The nucleic acid detection of RT-PCR is performed with throat swabs, and the cycle threshold (Ct) is collected.

2.3. Detection of serum cytokines and chemokines

Detection of 34 cytokines and chemokines in serum by multi-cytokine detection system, including $IFN-\alpha$, $IFN-\gamma$, $TNF-\alpha$, $TNF-\beta$, $IL-1\alpha$, $IL-1RA$, $IL-1\beta$, $IL-2$, $IL-4$, $IL-5$, $IL-6$, $IL-7$, $IL-8$, $IL-9$, $IL-10$, $IL-12p70$, $IL-13$, $IL-15$, $IL-17A$, $IL-18$, $IL-21$, $IL-22$, $IL-23$, $IL-27$, $IL-31$, granulocyte-macrophage colony stimulating factor (GM-CSF), eosinophil chemoattractant protein (eotaxin), growth-regulating oncogenic-α (GR0-α), interferon-inducible protein-10 (IP-10), monocyte chemokine (MCP-1), macrophage inflammatory protein (MIP)-1α, $MIP-1\beta$, stromal cell derived factor-1α (SDF-1α), regulated activated normal T cells expression and secretion (RANTES).

3. Least weighted whale optimized algorithm mixed kernel SVM(LWWOA-MSVM)

In this paper, a mixed kernel support vector machine based on the fusion of polynomial kernel and Gaussian kernel is proposed. Aiming at the shortcomings of basic WOA, such as easy to fall into local extreme value and slow convergence speed, this paper realizes the improvement of WOA by introducing nonlinear factors and adaptive weights. Then the improved algorithm is used to optimize the parameters of MSVM. The LXWOA-MSVM autonomous diagnosis prediction model for COVID-19 is proposed.

3.1. Basic whale optimization algorithm

The whale optimization algorithm is a heuristic search algorithm that imitates the hunting strategy of humpback whales [43]. It includes three links: the prey being surrounded, attacking with bubble net and prey being searched.

3.1.1. Prey surrounded

When the prey is surrounded, the position of the whale nearest to the prey is equivalent to a local optimal solution, and other whales are updated according to the optimal whale position to surround the prey [44]. The update equation of whale position $X(t)$ and the distance

D between the whale position and the optimal whale position are expressed as:

$$X(t+1) = X^*(t) - A^* \cdot D \tag{6}$$

$$D = |C \cdot X^*(t) - X(t)| \tag{7}$$

where, t is the number of iterations; X^* is the best solution obtained so far; X is the current solution; A^* and C are matrix coefficients, expressed as:

$$A^* = 2a \cdot r - a \tag{8}$$

$$C = 2 \cdot r \tag{9}$$

where, r is a random vector in [0,1]; with the increase of t, a decreases linearly from 2 to 0, expressed as:

$$a = 2 - 2 \cdot \frac{t}{t_{Maxiter}} \tag{10}$$

where, $t_{Maxiter}$ is the maximum number of iterations.

3.1.2. Attack with bubble net

The whale spits out bubbles and swims to the target prey in a spiral trajectory [45]. The mathematical model for updating the individual position is:

$$X(t+1) = D \cdot e^{bl} \cdot \cos(2\pi l) + X^*(t) \tag{11}$$

where, D is the same as Eq. (7), b is a constant, and l is a random vector in $[0, 1]$.

3.1.3. Hunt for prey

At the stage of hunting for prey, whales wander for food and conduct global exploration randomly [46]. The mathematical model is:

$$X(t+1) = X_{rand}(t) - A^* \cdot D \tag{12}$$

$$D = |C \cdot X_{rand}(t) - X(t)| \tag{13}$$

where, X_{rand} represents the location where the whale randomly selects an individual from the population as the target position.

In WOA, when the parameters meet $|A^*| < 1$, the local optimal solution search is carried out. At this time, the whale surrounds the prey with the probability P^* and spirals with probability $1 - P^*$; When the parameters meet $|A^*| \geq 1$, the algorithm searches for the global optimal solution.

3.2. Least weighted whale optimization algorithm

3.2.1. Improved least convergence factor

In WOA, A^*-value determines the conversion between global search ability and local development ability of the algorithm, that is, the value change of the convergence factor a determines the optimization quality of the algorithm. However, a decreases linearly in the iterative process, which cannot adapt to the actual optimization process. This paper adopts a new least nonlinear exponential decreasing method for a:

$$a = 2 - 2\left(\frac{1}{e-1} \times \left(e^{\frac{t}{t_{Maxiter}}}\right) - 1\right) \tag{14}$$

The improved a decreases slowly in the early stage and it improves the global search ability. In the later stage, a decreases rapidly. The optimization speed is accelerated and the local search efficiency is improved.

3.2.2. Adaptive inertia weight

The value of inertia weight has an important influence on the optimization and convergence ability of the algorithm. In the traditional WOA, the inertia weight takes a large fixed value. Although it ensures the global optimization ability of WOA, it is not conducive to the local optimization in the later stage of WOA. Therefore, this paper divides the contraction encirclement and spiral predation behavior of WOA into three stages: early, middle and later. It adjusts the value of inertia weight according to the iteration period dynamically. The segmented dynamic inertia weight based on iteration period is:

$$w = \begin{cases} 1 - exp(rand(\frac{t}{t_{Maxiter}-1})), t \geq \frac{1}{3}t_{Maxiter} \\ 1, t < \frac{1}{3}t_{Maxiter} \end{cases} \tag{15}$$

where, $rand$ represents the random number between $0 \sim 1$; t represents the number of iterations and $t_{Maxiter}$ represents the maximum number of iterations.

In the early stage of WOA, w still maintains a large fixed value, so that the whale has a large search step. In the middle and later stages of WOA, as the iteration progresses, w-value decreases nonlinearly, making the whale approach the global optimal solution and speed up the convergence.

The value of inertia weight w is calculated according to Eq. (15), which ensures that w-value is within [0,1]. At the same time, with the implementation of WOA, w-value decreases nonlinearly, which is conducive to avoid the phenomenon that WOA falls into local optimization and cannot jump out in the later stage.

Through the cooperation of nonlinear convergence factor and adaptive weight, an improved whale optimization algorithm with high convergence accuracy and fast convergence speed is obtained. The location update equation of WOA is as following:

$$X(t+1) = wX^*(t) - A^* \cdot D, p < 0.5 \tag{16}$$

$$X(t+1) = D \cdot e^{bl} \cdot \cos(2\pi l) + wX^*(t), p \geq 0.5 \tag{17}$$

$$X(t+1) = wX_{rand}(t) - A^* \cdot D \tag{18}$$

3.3. Mixed kernel SVM

The regression of SVM uses the kernel function to map the data to the high-dimensional feature space, and then performs linear regression in the high-dimensional feature space [47]. According to the principle of structural risk minimization, the learning process is transformed into a convex optimization problem, namely:

$$min[\frac{1}{2}\|w\|^2 + c\sum_{i=1}^{l}(\xi_i + \xi_i^*)]$$
$$s.t.\begin{cases} y_i - w\Phi(x_i) - b^* \leq \varepsilon + \xi_i \\ -y_i + w\Phi(x_i) + b^* \leq \varepsilon + \xi_i^*, i = 1, 2, \ldots, l \\ \xi_i \geq 0, \xi_i^* \geq 0 \end{cases} \tag{19}$$

The final regression function is:

$$f(x) = \sum_{i=1}^{l}(a_i - a_i^*)K(x_i, x) + b^* \tag{20}$$

where, $\Phi(x)$ is a nonlinear mapping function; w is the normal vector of the hyperplane; b^* is the offset of the hyperplane; ε is the linear insensitive loss function; $K(x_i, x_j) = \Phi(x_i)\Phi(x_j)$ is the kernel function that satisfies the condition of Mercer. In this paper, the radial basis is selected as the kernel function of SVM. a_i and a_i^* are Lagrange multipliers in quadratic programming.

The polynomial kernel function is the local kernel function with strong fitting ability. The radial basis kernel function is the global kernel function with strong extrapolation ability. Therefore, the polynomial kernel and radial basis kernel are selected as the basis of

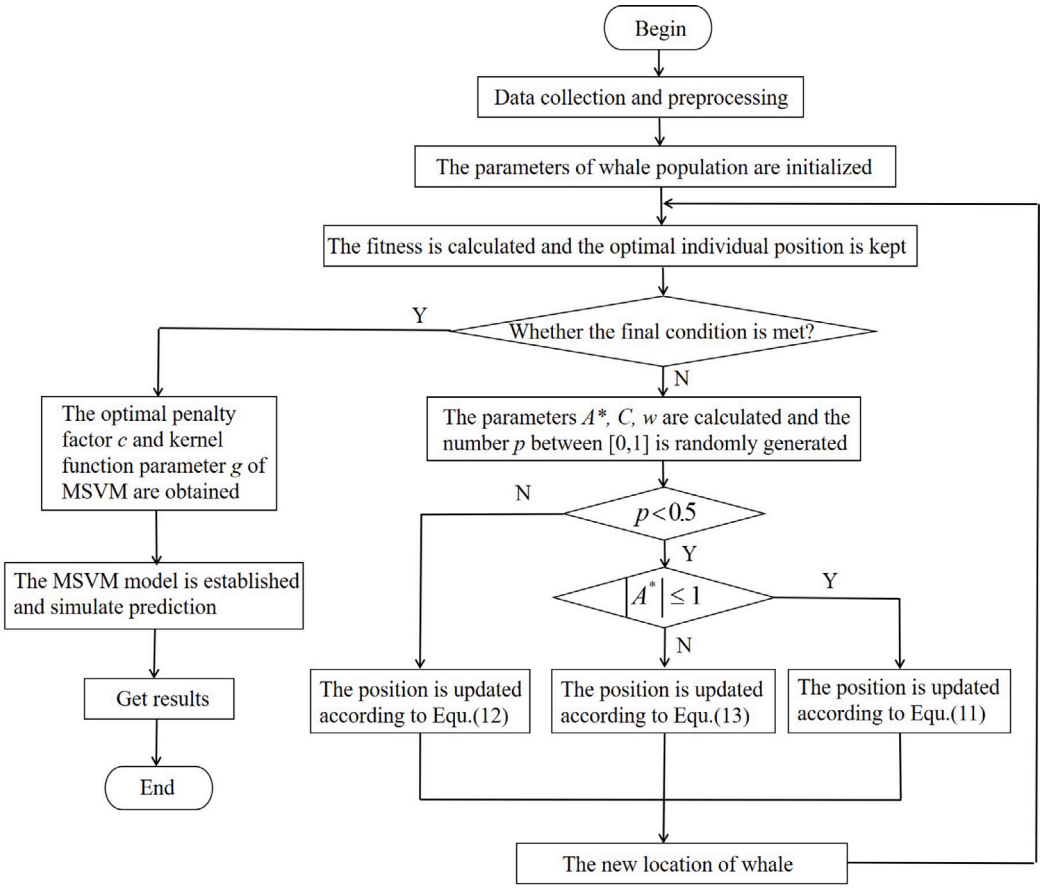

Fig. 3. The flowchart of LWWOA-MSVM algorithm for COVID-19 diagnosis.

the composite functions. According to the construction principle of the composite kernel function and the Mercer criterion, the following composite kernel function is constructed:

$$K_{min} = \frac{1}{2}[\rho K_{poly} + (1-\rho)K_{RBF} + K_{poly} \cdot K_{RBF}] \tag{21}$$

where, $K_{poly} = [g(x \cdot x_i) + 1]^3$ represents cubic polynomial kernel function; $K_{RBF} = exp(-g\|x - x_i\|^2)$, $g > 0$, it represents RBF kernel function; ρ represents the weight coefficient.

In Eq. (21), ρ-value determines the proportion of a single kernel function in the mixed kernel function. When $\rho > 0.5$, the polynomial kernel function is dominant. When $\rho < 0.5$, the Gaussian kernel function is dominant. In this paper, through repeated tests, $\rho = 0.35$.

3.4. The forecast implementation steps of LWWOA-MSVM

The key parameters of LWWOA optimized MSVM are penalty factor c, kernel function parameter g. The inertia weight of LWWOA proposed in this paper decreases with the increase of the number of iterations, so the complexity of the model is reduced and the amount of calculation is reduced. In addition, the optimized parameters by LWWOA are not many, which will reduce the model complexity of the algorithm and make it difficult to over fit. Fig. 3 shows the flowchart of LWWOA-MSVM algorithm for COVID-19 diagnosis. The prediction implementation steps can be summarized as following:

Step 1: the number of training and testing samples is determined. The search range of penalty factor c, kernel function parameter g are set. Eq. (22) is used to normalize the instance data sequence.

$$\hat{x} = (x - x_{min})/(x_{max} - x_{min}) \tag{22}$$

Step 2: the sum of the absolute value of the average relative error is selected as the fitness function of LXWOA-MSVM:

$$\begin{aligned} &minf(c,g) = |\sum_{i=1}^{n} \frac{|y_i - \hat{y}|}{y_i}| \\ &s.t. \begin{cases} c \in [c_{min}, c_{max}] \\ g \in [g_{min}, g_{max}] \end{cases} \end{aligned} \tag{23}$$

where, y_i is the measured value of the ith sample; $\hat{y}_i$ is the predicted value of the ith sample.

Step 3: the maximum number of iteration $t_{Maxiter}$, the population number N, the maximum inertia weight w_{max}, the minimum inertia weight w_{min} are set. The individual spatial position of the whale population is initialized and making the current iteration number $t = 1$.

Step 4: the fitness value of each whale and the population are calculated. The optimal individual position X^* in the population is found and recorded.

Step 5: the period of iteration. If $j \le t_{Maxiter}$, a, A^*, C, l and p are updated. When $p < 0.5$ and if $|A^*| < 1$, Eq. (16) is used to update the spatial position of the whale population. If $|A^*| \ge 1$, the position of the whale group X_{rand} from the current population is randomly determined, and Eq. (17) is used to update the spatial position of the whale population. If $p \ge 0.5$, Eq. (18) is used to update the spatial position of the current whale individual.

Step 6: the updated individual fitness value of the whale population is calculated. If the individual fitness of the new whale group is better than that of the previous generation, the individual position of the new whale group will replace that of the original group. Otherwise, the individual position of the original whale group is kept.

Step 7: $t = t + 1$ is set. Whether the algorithm meets the termination condition is judged. If so, the optimal individual position X^* and

its fitness value are output, and then the algorithm ends. Otherwise, step5∼ step7 are repeated.

Step 8: the optimal individual position X^* is obtained by LWWOA. That is, the penalty factor c, the kernel function parameter g are substituted into the LWWOA-MSVM model for prediction.

4. The measurement method of conflict evidence based on angle cosine and Lance distance

4.1. The identification framework and synthesis rules of traditional D-S evidence theory

In the theory of evidence, the combination of possible recognition results in pattern recognition is called the framework Θ, denoted as $\Theta = \{\theta_1, \theta_2 \cdots \theta_n\}$. θ represents the recognition result after evidence synthesis, which is called the focal element [48]. It is finite and countable, and they are mutually exclusive. The recognition framework is an important basis for pattern recognition, and the corresponding output results are obtained on the basis of evidence synthesis [49].

For the recognition framework Θ, 2^Θ is the set composed of all subsets of Θ, which satisfies $\phi \in 2^\Theta$ and $\Theta \in 2^\Theta$[50]. Under the identification framework Θ, the probability distribution function is the mapping of the set 2^Θ between [0,1], which is recorded as $m : 2^\Theta \rightarrow [0, 1]$ and satisfies:

$$\begin{cases} m(\phi) = 0 \\ \sum\limits_{\forall A \in 2^\Theta} m(A) = 1 \end{cases} \tag{24}$$

where, $m(A)$ represents the probability distribution function of the support degree for event A; A indicates a specific event; $m(\phi)$ indicates the support degree of the evidence for uncertain empty sets.

$m(A)$ is the basic probability distribution of an eigenvalue to proposition A, which indicates the degree of support for proposition A. If $m(A) > 0$, A is called a focal element of the function.

Under the same recognition framework, the fusion rule of probability distribution function is defined as:

$$m(A) = \frac{1}{1-k} \cdot \sum_{\cap A_s = A} \prod_{1 \le i \le n} m_i(A_s) \quad (0 < i \le n) \tag{25}$$

$$k = \sum_{\cap A_s = \varnothing} \prod_{1 \le i \le n} m_i(A_s) \tag{26}$$

where, n represents the total number of probability distribution function; $m_i(A_s)$ represents the confidence level of the event A_s in the ith probability distribution function; k represents the fusion conflict factor, which reflects the degree of conflict in the probability distribution function fusion. The greater k-value, the greater the conflict between different evidences.

4.2. Problems in D-S evidence theory

Although D-S evidence theory has many advantages, it can generally deal with uncertain information in multi-modal system well. However, when it integrates highly conflicting evidence, the D-S evidence theory has the problem of failure. Mainly as: (1) It has the problem of one-vote veto. No matter how much other evidences support the proposition, when the basic trust distribution function of a certain evidence is 0, the occurrence of this proposition is completely denied. (2) It has a normalization factor. When $k = 1$ can be obtained from the D-S synthesis equation, the denominator of $\frac{1}{1-k}$ is 0. At this time, the fraction is meaningless and the D-S evidence theory cannot be used. (3) It has the poor robustness. Even if there is a slight change in the degree of support for the proposition, it will seriously affect the whole synthesis result.

In view of the problems existing in the above-mentioned D-S evidence theory, this paper uses the cosine of the included angle and the Lance distance to measure the degree of the evidence conflict, so as to reduce the incorrect conclusion due to the conflict between different evidences.

4.3. An improved D-S evidence fusion method based on angle cosine and Lance distance

This paper modifies the source of evidence in the D-S evidence theory. Firstly, whether there is conflict between different evidences is judged. If there is no conflict, D-S synthesis rule is directly used; If it exists, the Lance distance between different evidences under the identification framework Θ is calculated and the reliability of each evidence is determined. Then, the basic trust function is redistributed with the reliability as the weight. Finally, the weighted average evidence is fused by D-S synthesis rules to get the final result.

4.3.1. Conflicting and non-conflicting evidences are determined

There are N evidences are supposed under the recognition framework Θ. The basic trust distribution functions of mutually independent evidences m_i and m_j can be expressed as $m_i = \{m_i(H_1), m_i(H_2), \ldots, m_i(H_M)\}$ and $m_j = \{m_j(H_1), m_j(H_2), \ldots, m_j(H_M)\}$. Then the similarity between the evidences m_i and m_j is expressed by the angle cosine function as:

$$s_{ij} = cos_{m_i m_j} = \frac{\langle m_i \cdot m_j \rangle}{|m_i| \cdot |m_j|} = \frac{\sum_{t=1}^{M} m_{it} \cdot m_{jt}}{\sqrt{\sum_{t=1}^{M} m_{it}^2} \cdot \sqrt{\sum_{t=1}^{M} m_{jt}^2}} \tag{27}$$

According to the angle cosine equation, when the value of cosine between two evidences is 1, it indicates that the two evidences are completely consistent. According to the properties of the cosine function, with the angle increases, the value of cosine becomes smaller and smaller, then the conflict between different evidences will gradually increase. When the included angle increases to 90°, there is no correlation between the evidences. In particular, when the cosine value of the two evidences is equal to −1 and the included angle is 180°, there is no correlation between the evidences at all.

In order to judge whether there is conflict between different evidences, the average similarity between one evidence and other evidences is obtained to quantify the similarity between the evidences.

$$\overline{S} = \begin{bmatrix} \overline{s_1} \\ \overline{s_2} \\ \vdots \\ \overline{s_N} \end{bmatrix} \tag{28}$$

where, $\overline{s_i} = \frac{\sum_{j=1}^{M} s_{ij}}{M}$. On the basis of obtaining the average similarity, the set threshold τ is compared to determine whether there is a conflict between different evidences. When the similarity is less than the threshold τ, there is a conflict between the evidences and it is necessary to measure the conflict evidence. On the contrary, if there is no conflict between the evidences, the D-S composition rule can be used directly.

4.3.2. Measurement of the conflict evidence based on Lance distance

The traditional D-S evidence theory does not consider the correlation between the evidences and assigns the same weight to different evidences. However, due to various factors, the weights between different evidences are not necessarily the same. Because the Lance distance is suitable for large-scale data processing, this paper introduces it into D-S evidence theory. The large-scale data here refers to multi-modal data. Compared with a single diagnostic index, the multi-modal diagnostic index data belongs to large-scale data. The large scale here does not mean the number of huge, but it refers to the kind of many. According to the basic trust distribution function, the distance between different evidences is obtained, so as to make up for the defects of traditional evidence theory.

Assuming that in the system identification framework $\Theta = \{H_1, H_2, \ldots, H_M\}$, the Lance distance between evidences m_i and m_j is:

$$d_{ij}(L) = \frac{1}{M} \sum_{t=1}^{M} \frac{|m_{it} - m_{jt}|}{(m_{it} + m_{jt})} \tag{29}$$

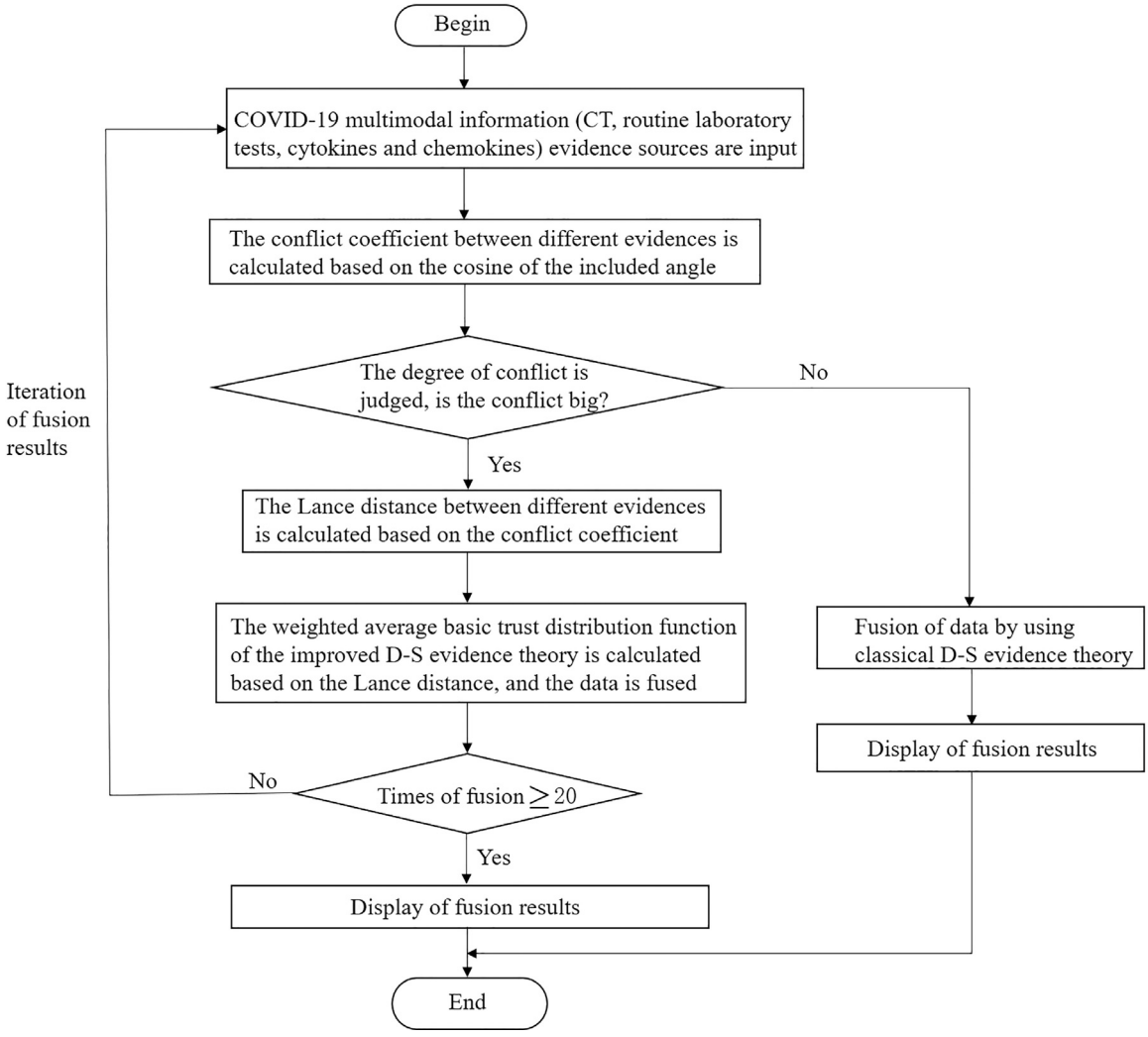

Fig. 4. The fusion process of improved D-S evidence theory.

According to the calculated Lance distance, the distance matrix $D_{N\times N}$ is:

$$D_{N\times N}=\begin{bmatrix} 0 & d_{12} & \cdots & d_{1N} \\ d_{21} & 0 & \cdots & d_{2N} \\ \vdots & \vdots & \vdots & \vdots \\ d_{N1} & d_{N2} & \cdots & 0 \end{bmatrix} \tag{30}$$

The distance of evidence can reflect the gap between the evidences. In order to take into account the fusion effect between the evidences, the consistency of evidences m_i and m_j is defined as:

$$coh(m_i,m_j)=1-D_{N\times N}=\begin{bmatrix} 1 & 1-d_{12} & \cdots & 1-d_{1N} \\ 1-d_{21} & 1 & \cdots & 1-d_{2N} \\ \vdots & \vdots & \vdots & \vdots \\ 1-d_{N1} & 1-d_{N2} & \cdots & 1 \end{bmatrix} \tag{31}$$

The degree of consistency between the evidences reflects the degree of mutual support. At this time, the reliability of an evidence m_i in the entire multi-modal system can be defined as:

$$rel=\frac{R_i}{\sum_{i=1}^{N} R_i} \tag{32}$$

Among them:

$$R_i=\sqrt{\sum_{j=1,j\neq i}^{N}(1-d_{ij})^2} \tag{33}$$

The more uncertain information contained in the evidence, the greater the uncertainty. Because different evidences have different proportions in the framework of the identification system, the reliability is used as the weight of the evidence to redistribute the basic trust distribution function of the evidence.

$$m_k'(H_i)=\begin{cases} rel_k\cdot m_k(H_i), H_i\neq\Theta \\ 1-\sum_{H_i\neq\varnothing} rel_k\cdot m_k(H_i), H_i=\Theta \end{cases} \tag{34}$$

After the basic trust distribution function is redistributed, a new piece of evidence is obtained based on the original evidence source by weighted average.

$$m_{ave}(H_i)=rel_1\times m_1(H_i)+rel_2\times m_2(H_i)+\cdots+rel_N\times m_N(H_i) \tag{35}$$

$m_{ave}(H_i)$ is used to replace the original trust distribution function, and D-S evidence theory is used to synthesize rules to fuse the replaced evidence. When there are N original evidences in the system, it is necessary to fuse $N-1$ times.

The method proposed in this paper considers the conflict evidence from two parts, and it uses the angle cosine function to judge the

conflict and non-conflict evidences in the system framework, which can reduce the computational complexity of the system to a certain extent. When there is conflict evidence in the system, it does not completely deny the possibility that contains the real information, but it assigns different weights to each evidence. Therefore, this method can improve the intuitive results due to the existence of conflict evidence to a certain extent. Fig. 4 shows the fusion process of improved D-S evidence theory.

5. Decision-level fusion for COVID-19 multi-modal recognition

The CT images, routine laboratory tests, serum cytokine and chemokine tests are independent of each other in multi-modal identification of COVID-19. Therefore, the ability of D-S theory to combine independent evidences can be used to fuse MSVM identification information from different features. Finally, the type of pneumonia (COVID −19 or viral pneumonia or bacterial pneumonia) is determined by the decision module. The algorithm steps are as following:

(1) MSVM recognition based on the single feature

CT images, routine laboratory tests, serum cytokine and chemokine tests of COVID-19 are extracted respectively. The MSVM classifier is used to recognize three kinds of single features.

(2) Construction of the BPA function

Because the decision output $f(x)$ of the standard MSVM is the hard output $\{1,-1\}$ and the soft decision of MSVM is required to solve the uncertainty problem, the most commonly used soft decision is probability. In order to construct the BPA of evidence, the sigmoid function is used as the connection function to map $f(x)$ to [0,1] to realize the posterior probability output of MSVM. The output form is:

$$P(y=1|x) \approx P_{A_S,B_S}(f) = \frac{1}{1+exp(A_S f + B_S)} \tag{36}$$

where f is $f(x)$, representing the standard output x-value in MSVM; A_S and B_S represent the parameters that control the shape of the sigmoid function. A_S and B_S can be obtained by solving the maximum likelihood problem, namely

$$\min_{Z=A_S,B_S} F(Z) = -[\sum_{i=1}^{l} t_i \lg p_i + (1-t_i)\lg(1-p_i)] \tag{37}$$

Among them, $p_i = P_{A_S,B_S}(f_i)$.

$$t_i = \begin{cases} \dfrac{N_+ + 1}{N_+ + 2}, (y_i = 1; i = 1,2,\ldots,l) \\ \dfrac{1}{N_- + 2}, (y_i = -1; i = 1,2,\ldots,l) \end{cases} \tag{38}$$

where, N_+ and N_- represent the number of positive and negative samples. For any two class $MSVMi$ classifier, after completing the learning process of the sample set, the optimal parameters A_S and B_S are obtained according to Eq. (36), and the posterior probability p_j is constructed. Then the learning sample set $MSVMi(i = 0,1,2)$ is tested to obtain the recognition accuracy r_i. The BPA function can be defined as:

$$m_j(A) = p_j r_j \tag{39}$$

(3) Decision fusion and judgment rules

The reliability of each evidence is calculated according to Eq. (39), and the reliability under the combined effect of these evidences is calculated according to Eq. (35). $A_i(i = 0,1,2)$ is the type of pneumonia (COVID-19 or viral pneumonia or bacterial pneumonia), and A_w is the target category (COVID −19 or viral pneumonia or bacterial pneumonia). After obtaining the evidence A_i in the framework Θ and the uncertainty evidence $m_j(\Theta)$, the classification decision is subject to the following rules: (I) $m(A_w) = max\{m(A_i)\}$. That is, the class with the greatest reliability is the target class; (II) $m(A_w) - m(A_i) > \varepsilon_1(\varepsilon_1 > 0)$. That is, the difference of reliability between the target class and other classes must be greater than a certain threshold; (III) $m(A_w) - m(\Theta) > \varepsilon_2(\varepsilon_2 > 0)$. That is, the reliability of the target class must be greater than the uncertain reliability assignment. (IV) $m(\Theta) < \theta(\theta > 0)$. That is, the assigned value of uncertainty reliability must be less than a certain threshold and the uncertainty of evidence for the target class cannot be too large.

6. Simulation and analysis of results

The software and hardware environment involved in this experiment are as following:

Software environment: Windows 10 operating system, Matlab R2019b, ImageJ 1.48u.

Hardware environment: Intel Core i54670–3.4 GHz, 8.0 Gbyte RAM, 500 Gbyte hard disk.

Experimental data: the CT images of 450 patients with GGO labeled by doctors (including 150 cases of COVID-19, 150 cases of bacterial pneumonia, 150 cases of viral pneumonia) are used as the experimental samples, with the size of 512 ×512, and the thickness is 2 mm. At the same time, routine laboratory indexes, serum cytokines and chemokines are collected from these 450 patients. The COVID-19 CT images, routine laboratory indexes, serum cytokines and chemokines tested in this paper are from Chinese PLA general hospital. In this study, the pathological indicators(CT, routine laboratory indexes, serum cytokines and chemokines) of 360 patients(including 120 cases of COVID-19, 120 cases of bacterial pneumonia, 120 cases of viral pneumonia) are used as the original data to construct the detection model, and then the pathological indicators(CT, routine laboratory indexes, serum cytokines and chemokines) of 90 patients(including 30 cases of COVID-19, 30 cases of bacterial pneumonia, 30 cases of viral pneumonia) are used as the detection data to verify the validity of the model. The existing COVID-19 autonomous diagnosis system is mainly based on CT image [51], and no scholar has proposed to use multi-modal indicators (routine laboratory testing, cytokines and chemokines testing, CT image) for autonomous diagnosis of COVID-19. Therefore, such public multi-modal data sources are not easy to find. Limited by the cost and difficulty of collection, the data of the experimental samples in this paper were all collected from the hospital. The amount of data used in this paper is what we have tried our best to collect.

The parameters are set as following: the maximum number of iterations of LWWOA-MSVM $t_{Maxiter} = 200$, the number of groups $N = 20$, the constant $b = 2$, the linear inductive loss function $\varepsilon = 1.5$, the weight coefficient $\rho = 0.35$.

The evaluation indexes of COVID-19 classification model include accuracy, precision. The equations are as following:

$$Accuracy = \frac{TP + TN}{TP + TN + FP + FN} \tag{40}$$

$$Precision = \frac{TP}{TP + FP} \tag{41}$$

where, TP represents the number of correctly classified COVID-19; FP represents the number of misclassified COVID-19; TN represents the number of correctly classified non COVID-19; FN represents the number of misclassified non COVID-19.

6.1. Target attribute information of COVID-19 diagnostic indicators

In this paper, three groups $(e1, e2, e3)$ of diagnostic indicators are used, including the detection of CT image indicators, routine laboratory indicators, serum cytokine and chemokine tests. 58 kinds of attribute information are collected for three targets (bacterial pneumonia, COVID-19 and viral pneumonia). $P < 0.05$ is considered to be statistically significant. The COVID-19, bacterial pneumonia, and viral pneumonia are all advanced types in this paper. Table 3 shows CT image detection results (gold standard) of GGO for COVID-19 and suspected cases. Table 4 shows laboratory test results (gold standard) of COVID-19 and suspected cases. Table 5 shows detection results (gold standard) of serum cytokines and chemokines for COVID-19 and suspected cases.

Table 3
CT image detection results (gold standard) of GGO for COVID-19 and suspected cases.

Feature category	Feature component	Bacterial pneumonia	COVID-19	Viral pneumonia	*P*-value
Shape feature	perimeter	9.07 ± 1.74	9.56 ± 0.24	10.36 ± 2.09	0.075
	area	1.50 ± 0.18	1.59 ± 0.21	1.70 ± 0.20	0.082
	volume	2.71 ± 0.24	2.84 ± 0.22	2.94 ± 0.28	1.524
	circularity	0.3121 ± 0.2414	0.6517 ± 0.3525	0.9532 ± 0.4925	0.067
	rectangularity	0.3625 ± 0.1352	0.6961 ± 0.3562	0.9659 ± 0.4462	0.062
	extension length	0.2141 ± 0.1241	0.3529 ± 0.2125	0.6432 ± 0.3251	0.059
	number of Euler	9 ± 4	10 ± 3	13 ± 6	0.563
	number of corners	12 ± 7	15 ± 5	17 ± 7	0.064
	first-order Hu moment	2.72 ± 0.12	4.24 ± 0.24	7.86 ± 0.35	0.071
	second-order Hu moment	4.31 ± 0.14	6.86 ± 0.25	8.32 ± 0.31	0.151
Intensity feature	intensity mean	5.23 ± 1.05	5.90 ± 1.24	7.07 ± 1.74	0.621
	intensity variance	9.41 ± 2.63	14.06 ± 3.63	16.88 ± 4.21	0.164
	skewness	0.3525 ± 0.1512	0.5956 ± 0.3241	0.7532 ± 0.3351	0.251
	kurtosis	1.6743 ± 0.6425	2.7348 ± 1.4143	3.5 ± 1.7532	0.531
	maximum and minimum intensity difference	4.86 ± 1.36	5.51 ± 1.56	6.56 ± 2.04	0.769
	intensity gradient	0.4625 ± 0.2452	0.5636 ± 0.2853	0.6734 ± 0.3824	0.062
	Laplace divergence(mean)	10.4593 ± 2.4913	13.9598 ± 3.5921	15.8426 ± 4.6925	0.314
	Laplace divergence(difference)	6.80 ± 1.56	7.29 ± 1.34	8.03 ± 1.69	0.224
Texture feature	*con*	6.4352 ± 3.4235	8.3104 ± 4.6436	10.5637 ± 5.4522	0.124
	relevance	9.4534 ± 3.3411	12.0416 ± 4.5631	15.3421 ± 5.3212	0.393
	Ent	0.3432 ± 0.1943	0.4303 ± 0.2452	0.5492 ± 0.3521	0.486
	IDM	0.6436 ± 0.2414	0.7709 ± 0.4625	0.8231 ± 0.4692	0.12

Table 4
Laboratory test results (gold standard) of COVID-19 and suspected cases.

index	bacterial pneumonia	COVID-19	viral pneumonia	*P*-value
WBC ($\times 10^9$/L)	7.62 ± 3.70	5.01 ± 1.43	3.80 ± 1.10	0.024
L ($\times 10^9$/L)	3.06 ± 0.84	1.60 ± 0.45	0.96 ± 0.27	<0.001
N ($\times 10^9$/L)	4.06 ± 3.62	3.09 ± 1.31	2.50 ± 0.80	0.76
Hb (g/L)	144.00(128.25,161.25)	142.50(121,155.25)	132.00(109.00,135.50)	0.26
ALT (U/L)	13.25(10.83,42.30)	20.25(13.65,31.30)	24.50(12.10,55.50)	0.72
AST (U/L)	31.65(23.98,37.45)	23.25(19.75,30.38)	34.50(24.80,51.20)	0.24
T-Bil (u mol/L)	13.95(10.00,46.85)	10.20(7.95,13.75)	6.40(5.55,7.75)	0.01
GGT (U/L)	14.55 ± 2.78	22.52 ± 10.26	19.74 ± 12.20	0.40
Alb (g/L)	47.48 ± 2.34	45.47 ± 4.64	40.66 ± 3.22	0.047
ChE (U/L)	10719.25 ± 1447.10	7980.10 ± 2339.50	6792.40 ± 1524.63	0.03
ALP (U/L)	47.10(45.45,49.88)	50.45(47.13,72.65)	55.40(47.45,75.95)	0.37
CRP (mg/L)	0.03(0.01,0.05)	3.25(0.11,14.04)	14.66(7.66,35.37)	0.02
LDH (U/L)	207.50(183.00,223.00)	172.50(151.00,220.75)	201.00(166.00,232.50)	0.84
$CD3^+T$ (/uL)	2106.25 ± 605.95	1140.58 ± 380.42	580.00 ± 314.15	<0.001
$CD4^+T$ (/uL)	852.25 ± 230.37	566.00 ± 231.59	334.20 ± 177.00	0.009
TT (s)	18.33 ± 0.87	17.61 ± 0.65	17.00 ± 0.62	0.048
PT (s)	11.20 ± 0.51	11.65 ± 0.65	11.78 ± 0.64	0.37
Fib (g/L)	2.78(1.93,2.86)	2.61(2.07,3.12)	2.64(2.19,4.00)	0.86
APTT (s)	25.95 ± 1.68	28.44 ± 3.37	29.14 ± 3.66	0.31
D-Dimer (mg/L)	0.62(0.19,1.10)	0.26(0.21,0.37)	0.27(0.22,0.31)	0.95
Glu (mmol/L)	5.66(4.70,6.92)	5.65(5.30,7.10)	7.18(6.00,9.79)	0.13
Ca2+ (mmol/L)	2.40 ± 0.11	2.25 ± 0.16	2.13 ± 0.10	0.036
TC (mmol/L)	4.65(3.36,5.00)	4.00(3.59,4.27)	3.64(3.15,4.03)	0.28
TG (mmol/L)	0.88(0.64,2.92)	0.89(0.73,1.27)	1.07(0.95,1.18)	0.61
Ct	<37	≥40	37~40	<0.001

Table 5
Detection results (gold standard) of serum cytokines and chemokines for COVID-19 and suspected cases.

index	bacterial pneumonia	COVID-19	viral pneumonia	*P*-value
IL-7 (pg/mL)	7.33 ± 2.83	12.71 ± 2.14	16.73 ± 2.13	0.018
IL-8 (pg/mL)	18.31 ± 10.58	223.51 ± 158.68	173.38 ± 158.69	0.003
IL-18 (pg/mL)	35.34(18.74,39.20)	39.59(22.00,61.49)	41.13(18.25,123.47)	0.253
eotaxin (pg/mL)	15.52 ± 10.43	13.66 ± 11.83	10.29 ± 7.88	0.945
GRO-α (pg/mL)	9.56 ± 6.82	26.35 ± 22.94	10.43 ± 6.52	0.166
IP-10 (pg/mL)	38.4 ± 18.94	129.89 ± 122.89	169.47 ± 139.98	0.053
MCP-1 (pg/mL)	13.95(10.00,46.85)	10.20(7.95,13.75)	6.40(5.55,7.75)	0.01
MIP-1α (pg/mL)	14.55 ± 2.78	22.52 ± 10.26	19.74 ± 12.20	0.40
MIP-1β (pg/mL)	47.48 ± 2.34	45.47 ± 4.64	40.66 ± 3.22	0.047
SDF-1α (pg/mL)	107.19 ± 14.47	79.80 ± 23.39	67.92 ± 15.24	0.03
RANTES (pg/mL)	47.10(45.45,49.88)	50.45(47.13,72.65)	55.40(47.45,75.95)	0.37

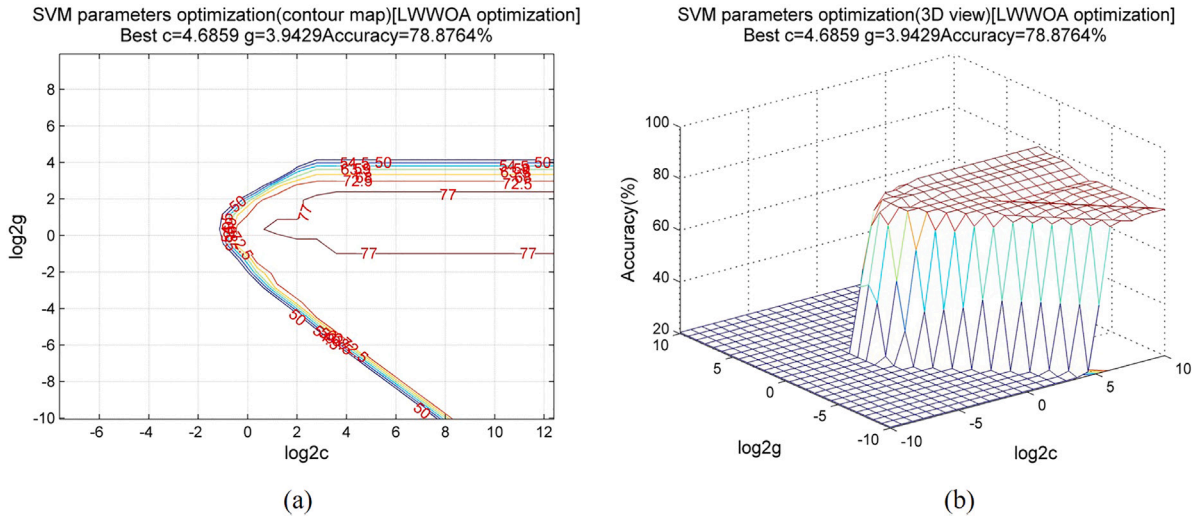

Fig. 5. Parameter selection results of COVID-19 CT image classification model (a) contour map; (b) 3D view.

6.2. Parameters optimization of LWWOA-MSVM classification model for COVID-19

In order to verify the COVID-19 classification effect of the improved algorithm, LWWOA-MSVM (paper method), traditional whale optimization algorithm-mixed support vector machine (TWOA-MSVM) [52], genetic algorithm-mixed support vector machine (GA-MSVM) [53] and particle swarm optimization- mixed support vector machine (PSO-MSVM) [54] models are used to train the data of CT images, routine laboratory indexes, serum cytokines and chemokines, and then COVID-19, bacterial pneumonia and virtual pneumonia are classified by the tested data.

The CT dataset of COVID-19 is classified. The upper and lower limits of parameters c and g are determined by LWWOA for large-scale optimization. The contour map of MSVM parameters selection based on LWWOA is shown in Fig. 5. According to Fig. 5, the range of parameter c is reduced to $2^0 \sim 2^4$, that is $1 \sim 16$; the range of parameter g is reduced to $2^{-1} \sim 2^3$, that is $0.5 \sim 8$. The maximum number of iterations of LWWOA is set to 200 and the number of population is 20. According to the rough range obtained by optimization, the search range of parameters c and g are set to be [1, 16], [0.5, 8] respectively. After the training of LWWOA-MSVM classification model, the best optimization parameters are obtained as best c=4.6859, best g=3.9429. That is, the best fitness score of the model is the highest at this time. In order to judge the performance of the model, the MSVM classification model optimized by TWOA, GA and PSO are selected for comparison with LWWOA-MSVM. The same maximum number of iterations and population size are set. The optimization process of the four optimization algorithms are shown in Fig. 6. It can be seen that compared with the three optimization algorithms of TWOA, GA, and PSO, the LWWOA-MSVM classification model has the highest fitness score of 78.8764%. The optimal fitness scores of the MSVM classification model optimized by TWOA, GA and PSO are 70.2399%, 67.117% and 65.0221% respectively. The optimization speed of LWWOA is fast, and the fitness function value can reach the best when the number of iterations is 8. TWOA, GA, and PSO reached the optimal level at 37th, 25th and 20th generation respectively. Moreover, the LWWOA algorithm is relatively more stable and it is not easy to fall into the local optimum. The traditional comparison methods are easy to fall into the local optimum during the optimization process, and it falls into the local optimum solution in the 6th, 10th, and 18th generation.

The CT data of 90 samples are selected as the test set, including 30 cases of COVID-19, 30 cases of bacterial pneumonia, and 30 cases of viral pneumonia. The trained MSVM classification models are used to classify the CT dataset. The diagnostic results of COVID-19 of the four models are shown in Fig. 7. Among them, LWWOA-MSVM has the highest diagnostic classification precision of 78.89% (71/90). The diagnostic classification precision of TWOA-MSVM is 70% (63/90); the diagnostic classification precision of GA-MSVM is 66.67% (60/90), and the diagnostic classification precision of PSO-MSVM is 64.44% (58/90).

The routine laboratory test dataset of COVID-19 is classified. The upper and lower limits of parameters c and g are determined by LWWOA for large-scale optimization. The contour map of MSVM parameters selection based on LWWOA is shown in Fig. 8. According to Fig. 8, the range of parameter c is reduced to $2^1 \sim 2^4$, that is $2 \sim 16$; the range of parameter g is reduced to $2^1 \sim 2^2$, that is $2 \sim 4$. The maximum number of iteration of LWWOA is set to 200 and the number of populations is 20. According to the rough range obtained by optimization, the search range of parameters c and g are set to be [2, 16], [2, 4] respectively. After the training of LWWOA-MSVM classification model, the best optimization parameters are obtained as best c=5.8084, best g=3.7464. That is, the best fitness score of the model is the highest at this time. In order to judge the performance of the model, the MSVM classification model optimized by TWOA, GA and PSO are selected for comparison with LWWOA-MSVM. The same maximum number of iterations and population size are set. The optimization process of the four optimization algorithms are shown in Fig. 9. It can be seen that compared with the three optimization algorithms of TWOA, GA, and PSO, the LWWOA-MSVM classification model has the highest fitness score of 72.6419%. The optimal fitness scores of the MSVM classification model optimized by TWOA, GA and PSO are 66.12%, 69.0111% and 65.0221% respectively. The optimization speed of LWWOA is fast, and the fitness function value can reach the best when the number of iterations is 5. TWOA, GA, and PSO reached the optimal level at 18th, 12th and 23th generation respectively. Moreover, the LWWOA algorithm is relatively more stable and it is not easy to fall into the local optimum. The traditional comparison methods are easy to fall into the local optimum during the optimization process, and it falls into the local optimum solution in the 10th, 8th, and 9th generation.

The routine laboratory index of 90 samples are selected as the test set, including 30 cases of COVID-19, 30 cases of bacterial pneumonia, and 30 cases of viral pneumonia. The trained MSVM classification models are used to classify the routine laboratory index dataset. The

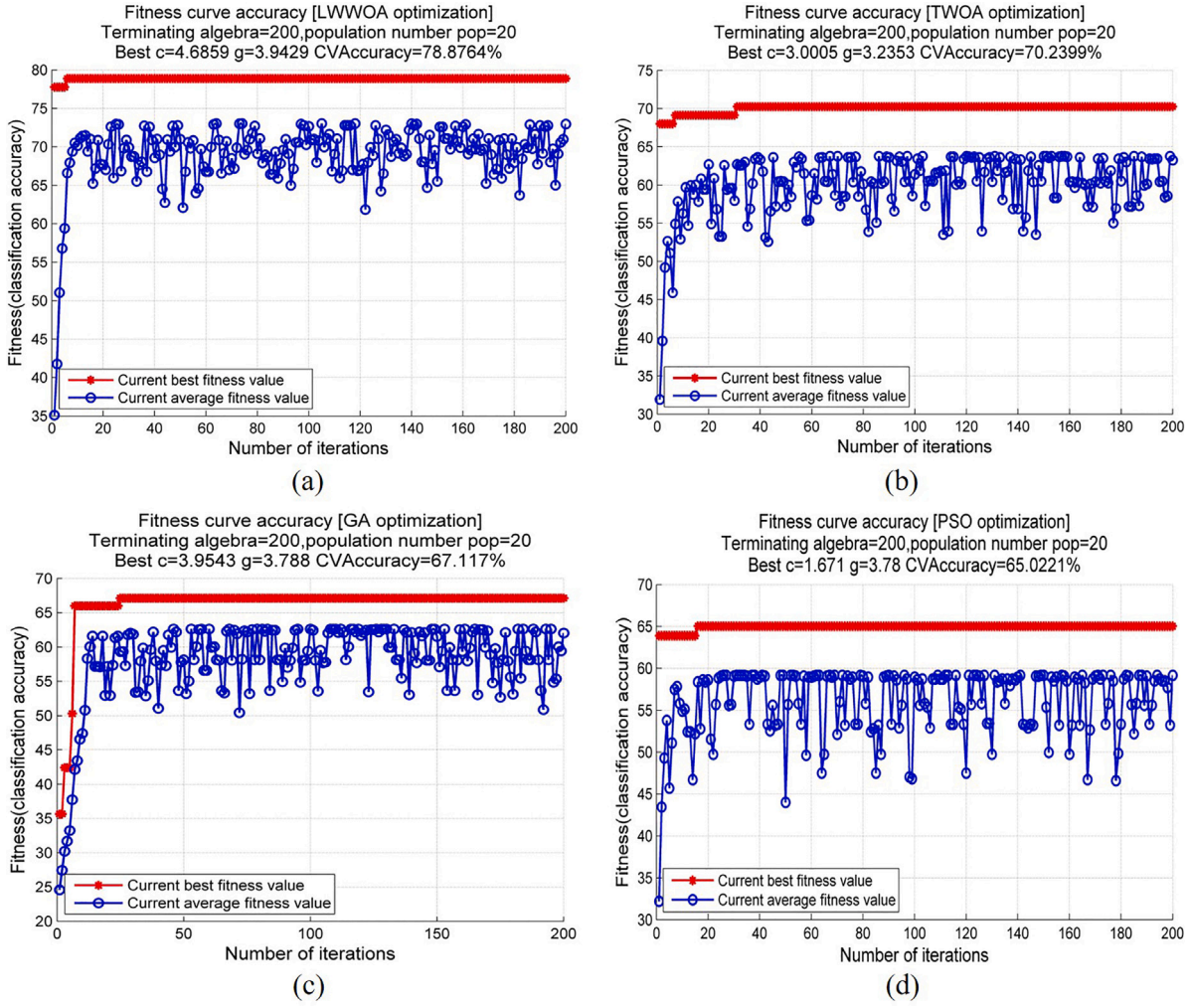

Fig. 6. COVID-19 CT image classification model parameter optimization fitness (accuracy) curve.

diagnostic results of COVID-19 of the four models are shown in Fig. 10. Among them, LWWOA-MSVM has the highest diagnostic classification precision of 73.33% (66/90). The diagnostic classification precision of TWOA-MSVM is 66.67% (60/90); the diagnostic classification precision of GA-MSVM is 68.89% (62/90), and the diagnostic classification precision of PSO-MSVM is 64.44% (58/90).

The serum cytokines and chemokines test dataset of COVID-19 is classified. The upper and lower limits of parameters c and g are determined by LWWOA for large-scale optimization. The contour map of MSVM parameters selection based on LWWOA is shown in Fig. 11. According to Fig. 11, the range of parameter c is reduced to $2^{-2} \sim 2^{0}$, that is $0.25 \sim 1$; the range of parameter g is reduced to $2^{0} \sim 2^{2}$, that is $1 \sim 4$. The maximum number of iterations of LWWOA is set to 200 and the number of population is 20. According to the rough range obtained by optimization, the search range of parameters c and g are set to be [0.25, 1], [1, 4] respectively. After the training of LWWOA-MSVM classification model, the best optimization parameters are obtained as best c=0.24471, best g=2.219. That is, the best fitness score of the model is the highest at this time. In order to judge the performance of the model, the MSVM classification model optimized by TWOA, GA and PSO are selected for comparison with LWWOA-MSVM. The same maximum number of iterations and population size are set. The optimization process of the four optimization algorithms are shown in Fig. 12. It can be seen that compared with the three optimization algorithms of TWOA, GA, and PSO, the LWWOA-MSVM classification model has the highest fitness score of 67.5066%. The optimal fitness scores of the MSVM classification model optimized by TWOA, GA and PSO are 61.6156%, 57.5153% and 53.3165% respectively. The optimization speed of LWWOA is fast, and the fitness function value can reach the best when the number of iterations is 20. TWOA, GA, and PSO reached the optimal level at 43th, 23th and 26th generation respectively. Moreover, the LWWOA algorithm is relatively more stable and it is not easy to fall into the local optimum. The traditional comparison methods are easy to fall into the local optimum during the optimization process, and it falls into the local optimum solution in the 6th, 8th, and 24th generation.

The serum cytokines and chemokines of 90 samples are selected as the test set, including 30 cases of COVID-19, 30 cases of bacterial pneumonia, and 30 cases of viral pneumonia. The trained MSVM classification models are used to classify the serum cytokines and chemokines dataset. The diagnostic results of COVID-19 of the four models are shown in Fig. 13. Among them, LWWOA-MSVM has the highest diagnostic classification precision of 67.78% (61/90). The diagnostic classification precision of TWOA-MSVM is 62.22% (56/90); the diagnostic classification precision of GA-MSVM is 57.78% (52/90), and the diagnostic classification precision of PSO-MSVM is 53.33% (48/90).

It can be seen from Table 6 that the accuracy and precision of LWWOA-MSVM are improved compared with the comparison methods, and the overall classification accuracy and precision can be improved to about 10%. However, the diagnostic classification samples have

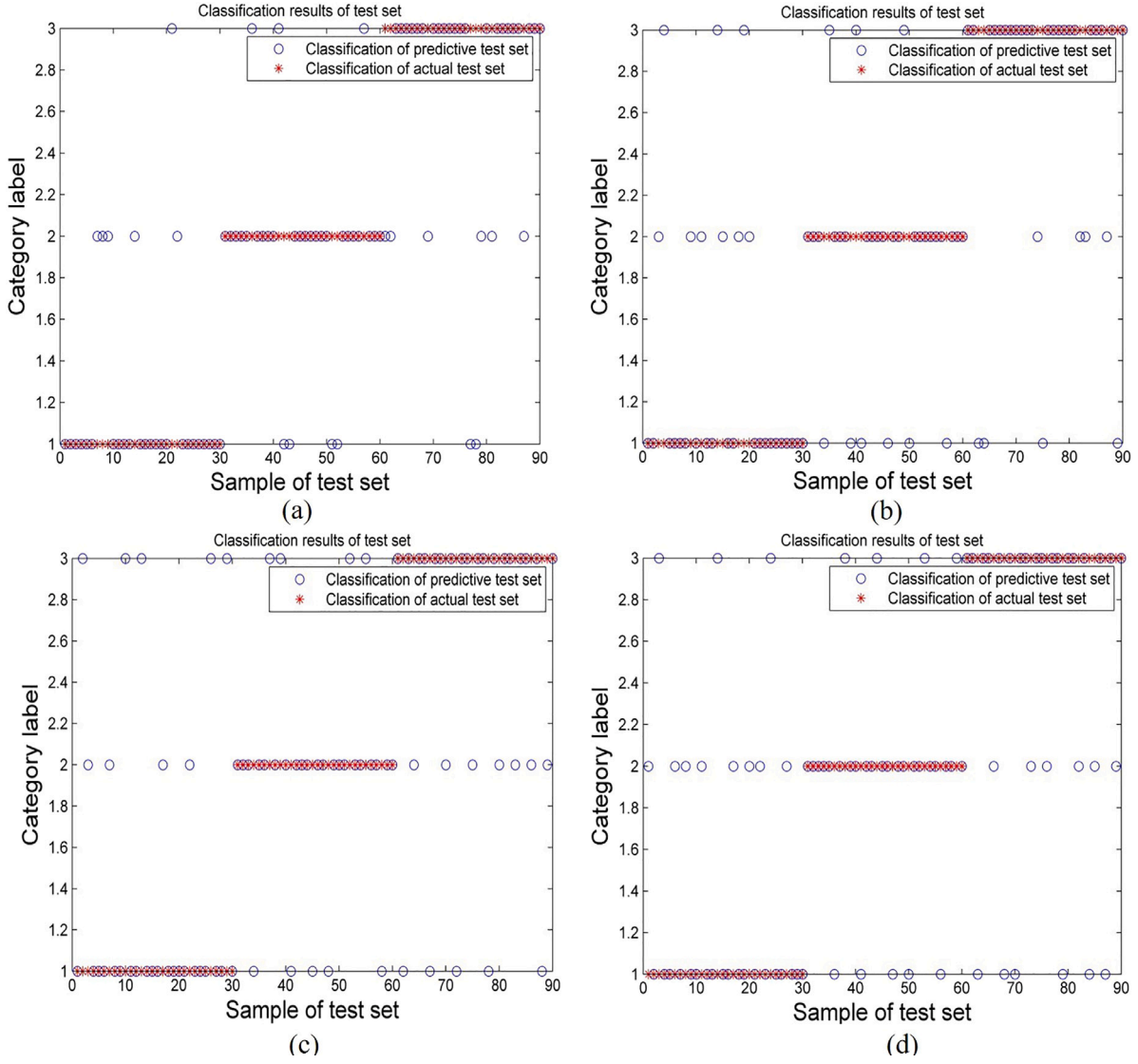

Fig. 7. Classification results of the COVID-19 CT image test set (precision).

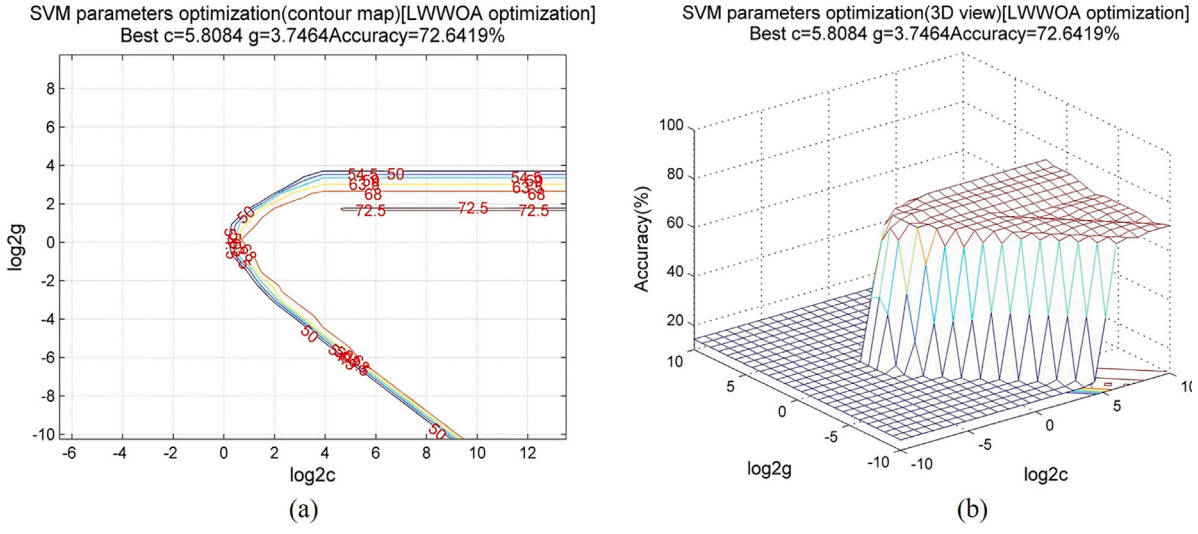

Fig. 8. Parameter selection results of COVID-19 routine laboratory index classification model (a) contour map; (b) 3D view.

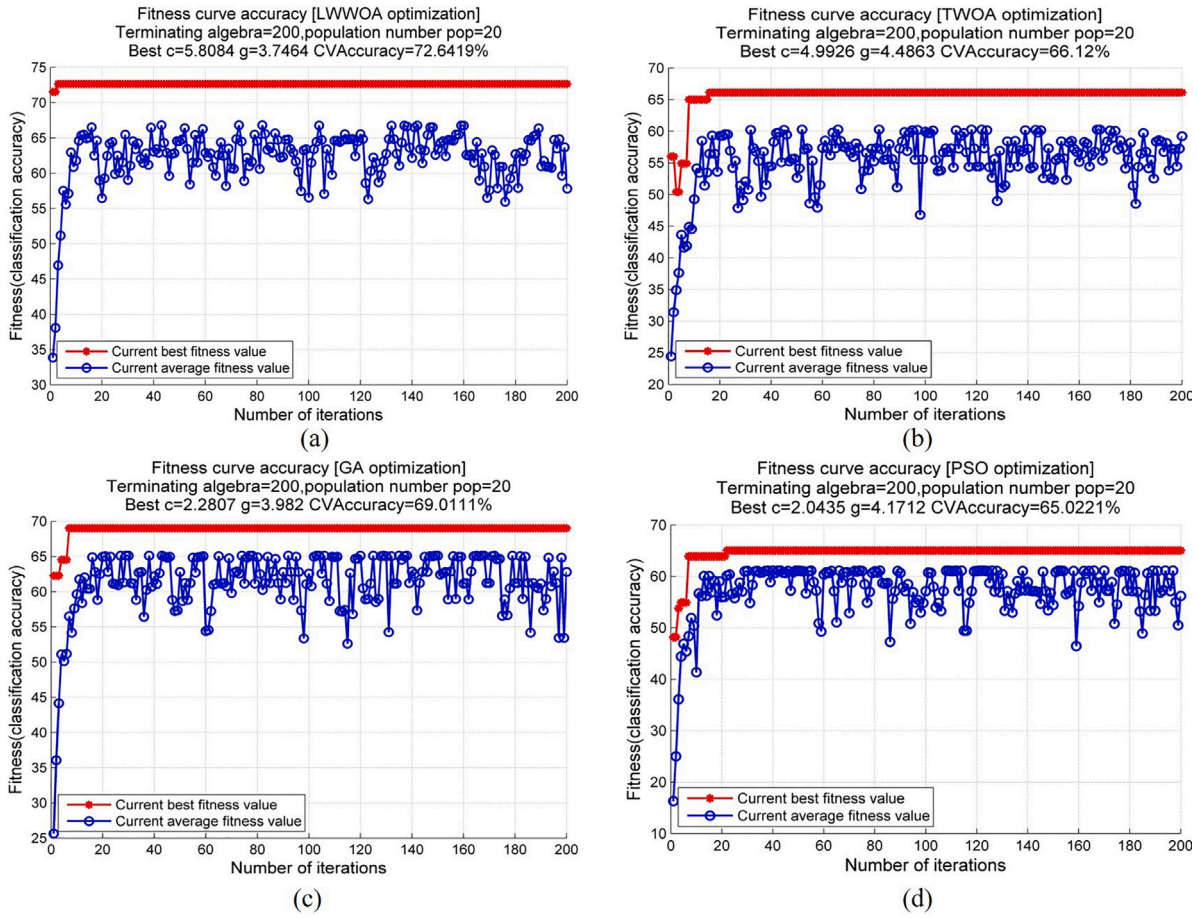

Fig. 9. COVID-19 routine laboratory index classification model parameter optimization fitness (accuracy) curve.

Table 6
Comparison of optimization parameters and classification evaluation indicators.

Types of diagnostic indicators	Classification methods	Optimal parameter c	Optimal parameter g	Test accuracy /%	Test precision /%
CT image	LWWOA-MSVM	4.6859	3.9429	78.8764	78.89
	TWOA-MSVM	3.0005	3.2353	70.2399	70.00
	GA-MSVM	3.9543	3.788	67.1170	66.67
	PSO-MSVM	1.671	3.78	65.0221	64.44
Routine laboratory indexes	LWWOA-MSVM	5.8084	3.7464	72.6419	73.33
	TWOA-MSVM	4.9926	4.4863	66.1200	66.67
	GA-MSVM	2.2807	3.982	69.0111	68.89
	PSO-MSVM	2.0435	4.1712	65.0221	64.44
Serum cytokines and chemokines	LWWOA-MSVM	0.24471	2.219	67.5066	67.78
	TWOA-MSVM	3.3351	0.7165	61.6156	62.22
	GA-MSVM	2.4733	0.9449	57.5153	57.78
	PSO-MSVM	18.7465	0.0828	53.3165	53.33

different degrees of misclassification, and the misclassification rate can exceed 20% for a certain type of index classification. Therefore, there is always a risk of misclassification when COVID-19 is classified only by a single index. Multiple indicator data should be integrated to obtain more credible evidence to reduce the risk of misclassification in the diagnosis of a single indicator source.

6.3. Solution of basic probability distribution function

The obtained three types of sensitive feature parameters are used as three sources of evidence, namely $e = \{e_1, e_1, e_1\}$. The basic recognition framework composed of three stages of pneumonia classification is $\Theta = \{m(A), m(B), m(C)\}$. The MSVM optimized by the whale algorithm is used for preliminary prediction to obtain the prediction error of each feature parameter, then the prediction error is subjected to locally judged and the decision result is converted into the posterior probability. Finally, the posterior probability is used to construct the basic probability distribution function of each feature parameter, as shown in Table 7.

It can be seen from Table 7 that the maximum value of the basic probability distribution function at stage I of evidence e3 is 0.5707, which appears at m(B), resulting in the misjudgment of the identification as stage II. The maximum value of the basic probability distribution function in the stage III of evidence e2 is 0.5971, which appears at m(B), resulting in the misjudgment of the identification as stage II. The maximum value of the basic probability distribution function in the stage I of evidence e1 is 0.7100, which appears at m(B), resulting in the misjudgment of the identification as stage II. Therefore, it is impossible to accurately identify COVID-19 and its suspected cases by a single diagnostic index.

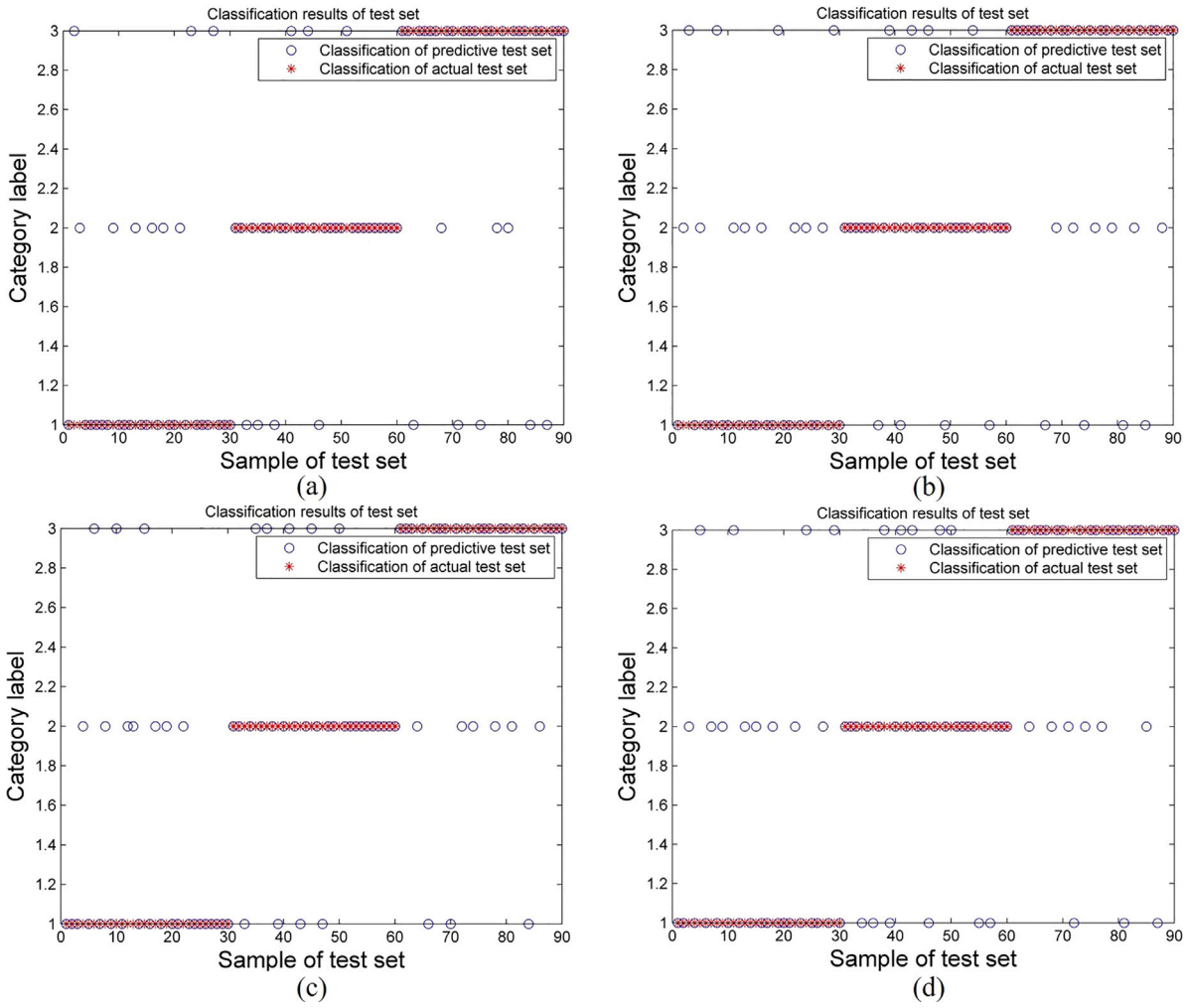

Fig. 10. Classification results of the COVID-19 routine laboratory index test set (precision).

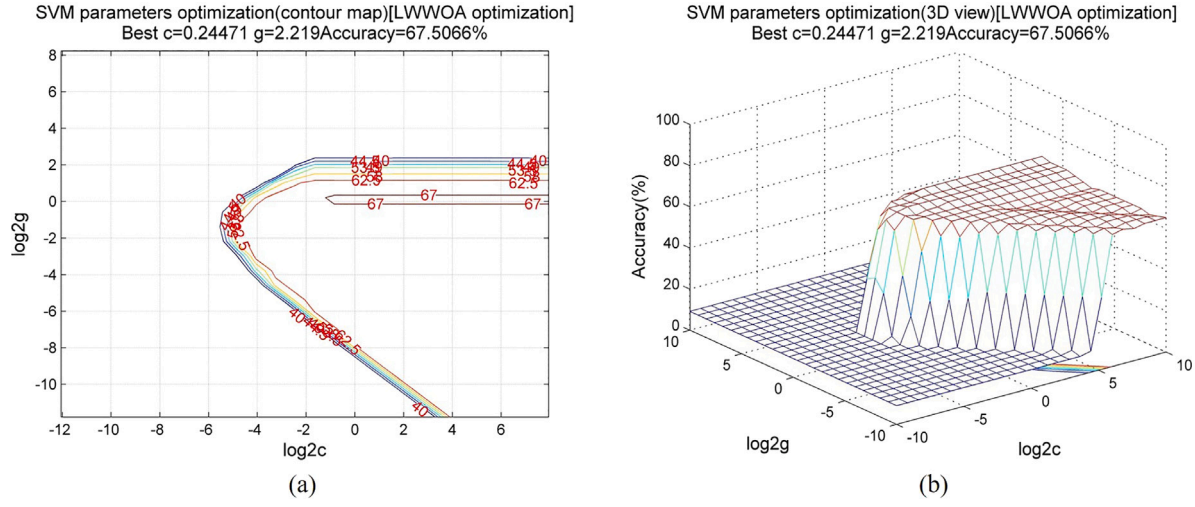

Fig. 11. Parameter selection results of COVID-19 serum cytokines and chemokines classification model (a) contour map; (b) 3D view.

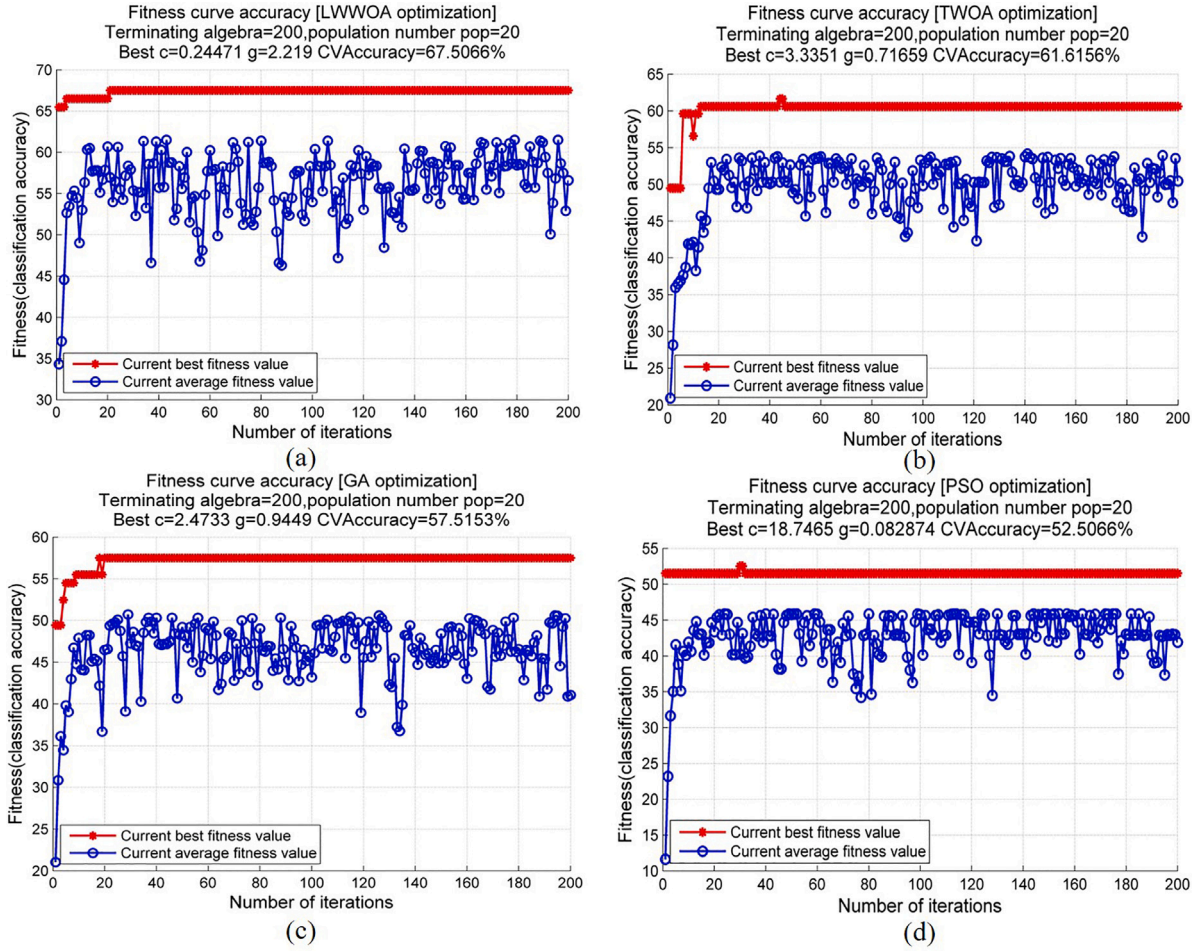

Fig. 12. COVID-19 serum cytokines and chemokines classification model parameter optimization fitness (accuracy) curve.

Table 7
Values of the basic probability distribution function and results of the preliminary identification in each evidence.

evidence	real stage	m(A)	m(B)	m(C)	recognition results
e_1	I	0.4078	0.7044	0.1026	II
	II	0.2539	0.6243	0.1615	II
	III	0.8393	0.0716	0.2208	I
e_2	I	0.3690	0.5801	0.1847	II
	II	0.2439	0.6317	0.1573	II
	III	0.0546	0.0953	0.7630	III
e_3	I	0.5078	0.5707	0.2797	II
	II	0.0835	0.7869	0.1026	II
	III	0.0583	0.1008	0.7501	III

6.4. Analysis of fusion results of multi-domain feature decision level

Aiming at the defect that a single feature has insufficient ability to identify COVID-19 and the suspected cases, the method of replacing single signal feature with multi-domain feature parameters is adopted. The traditional D-S evidence fusion and the weighted D-S evidence fusion methods are used to fuse three evidence sources respectively. The comparison of the recognition effect is shown in Table 8.

It can be seen from Table 8 that the recognition results of traditional D-S evidence fusion [55] and the weighted D-S evidence fusion are correct in stage I and II. However, in stage III, the recognition result of traditional D-S evidence fusion is wrong, while the recognition result of weighted D-S evidence fusion is correct. According to the evidence analysis of stage II and stage III, the more fusion evidence, the higher the value of the basic probability distribution function after fusion. Thus, the more fusion features, the higher the accuracy of prediction. Therefore, the COVID-19 prediction method based on the weighted D-S evidence theory and the multi-domain features proposed in this paper effectively solves the problem that it is difficult to accurately identify COVID −19 and suspected cases with a single pathological signal feature. It eliminates the defect of the traditional D-S evidence fusion method, that is, the recognition misjudgment caused by the failure of high conflict evidence fusion, and it provides an effective basis for COVID-19 autonomous diagnosis.

The data fusion of COVID-19 multimodal indicators can obtain more reliable diagnostic results. The classification results of three diagnostic index data fusion are shown in Fig. 14. As can be seen from Fig. 14, the multi-modal indicators classification precision of COVID-19 with the traditional D-S evidence theory fusion is 91.11% (82/90), and the multi-modal indicators classification precision of COVID-19 with the improved D-S evidence theory fusion is 97.78% (88/90). It shows that the new evidence obtained by fusion has high reliability, which can make the COVID −19 diagnostic classification results more stable and reliable, so as to effectively reduce the misclassification risk of a single diagnostic index.

The simulation results show that the proposed algorithm can effectively reduce the conflict between each evidence and the diagnosis conclusion, and it enhances the reliability of the correct diagnosis results. Compared with other comparison methods, it can solve the problem of high conflict of evidence. It quickly identifies COVID-19 and reduces uncertain information in the system with high reliability. It significantly improves the accuracy and precision of decision-making,

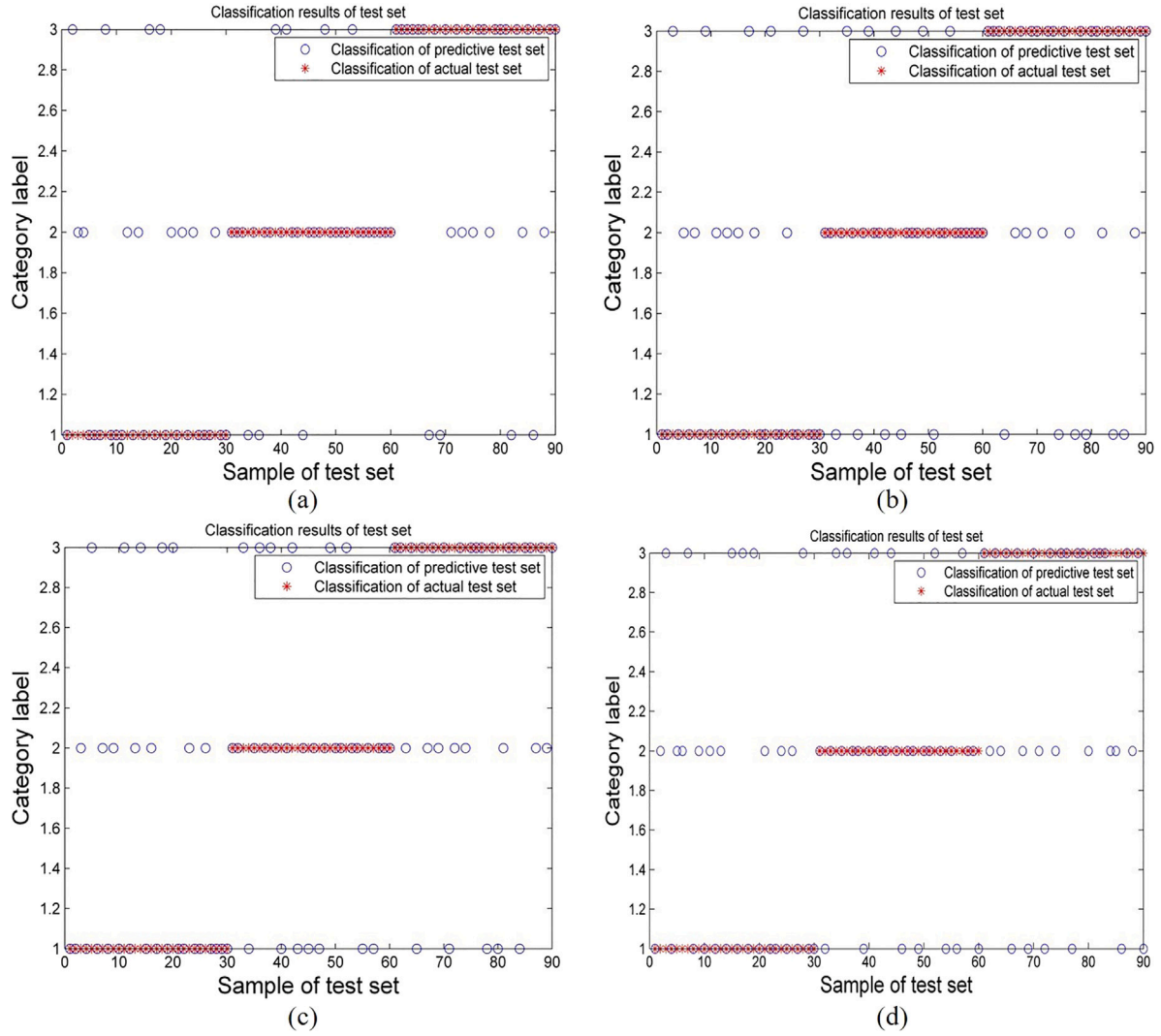

Fig. 13. Classification results of the COVID-19 serum cytokines and chemokines test set (precision).

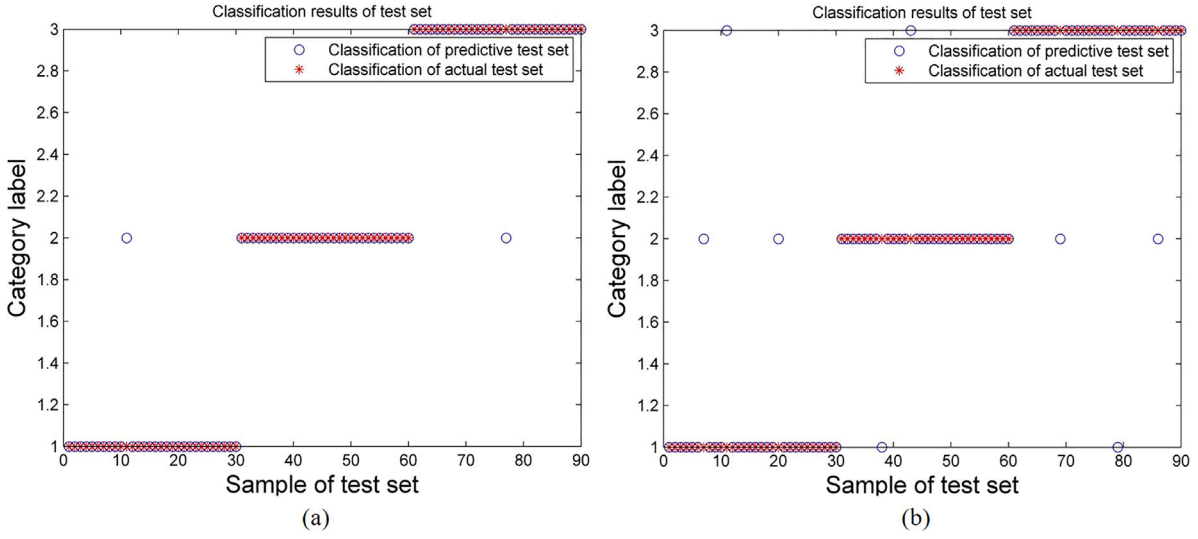

Fig. 14. COVID-19 classification precision by multi-modal indicators (a) LWWOA-MSVM combined with improved D-S evidence fusion; (b)LWWOA-MSVM combined with traditional D-S evidence fusion.

Table 8
Comparison of recognition results between traditional D-S evidence fusion and the improved D-S evidence fusion.

Real stage	Evidence fusion	Traditional D-S evidence fusion method				Improved D-S evidence fusion method			
		$m(A)_1$	$m(B)_1$	$m(C)_1$	Recognition result 1	$m(A)_2$	$m(B)_2$	$m(C)_2$	Recognition result 2
I	e_1,e_2	0.4456	0.4771	0.0933	II	0.6727	0.2255	0.0835	I
	e_1,e_3	0.0466	0.4408	0.4884	III	0.6786	0.2508	0.0651	I
	e_2,e_3	0.8220	0.1529	0.0243	I	0.7521	0.2108	0.0368	I
	e_1,e_2,e_3	0.7907	0.1898	0.0192	I	0.7265	0.2440	0.0291	I
II	e_1,e_2	0.1606	0.7413	0.0827	II	0.2047	0.6677	0.1078	II
	e_1,e_3	0.1142	0.4413	0.4433	III	0.0658	0.8901	0.0417	II
	e_2,e_3	0.0157	0.9705	0.0135	II	0.0352	0.9338	0.0304	II
	e_1,e_2,e_3	0.0049	0.9897	0.0053	II	0.0140	0.9707	0.0152	II
III	e_1,e_2	0.1238	0.4282	0.4457	II	0.0263	0.0547	0.8953	III
	e_1,e_3	0.1139	0.4091	0.4852	III	0.0101	0.0241	0.9608	III
	e_2,e_3	0.0014	0.0044	0.9938	III	0.0046	0.0143	0.9801	III
	e_1,e_2,e_3	0.0003	0.0013	0.9983	III	0.0014	0.0059	0.9925	III

and the experiment validates the effectiveness of multi-modal information fusion in COVID-19 autonomous diagnosis. The use of multi-modal indicators (CT, routine laboratory indexes, serum cytokines and chemokines) can effectively distinguish COVID-19 from viral pneumonia and bacterial pneumonia. However, the proposed method has some disadvantages. The LWWOA-MSVM treats each sample data equally, but each training data obviously has different effect on the calculation of the classification surface. Equal treatment will affect the calculation of the classification surface and thus affect the output of BPA, and the performance needs to be further improved. In addition, the COVID-19 multi-modal autonomous diagnosis system needs to collect multiple diagnostic indicators, so the cost of acquisition increases.

7. Conclusion

In this paper, the whale-optimized MSVM is used to establish a single-index classifier for COVID-19 based on CT images, routine laboratory index detection, serum cytokines and chemokines detection, and the output of each MSVM is used as independent evidence to construct the basic reliability distribution on this diagnostic index. Then, the improved D-S evidence theory is applied to effectively integrate the judgment information of COVID-19 from different diagnostic indicators as independent evidence at the decision-making level. Finally, the rules of constructed decision fusion threshold discrimination are used for decision recognition. The experimental results show that the paper method can not only avoid the problem of low recognition rate caused by the unilateralism of single diagnostic index, but it also solves the problem that the feature vector dimension is too high and is not conducive to the identification caused by the multi-diagnostic index features. However, the proposed method has some disadvantages. Multi-modal autonomous diagnosis system for COVID-19 needs to collect multiple diagnostic indicators, so the collection cost increases. MSVM needs to preliminarily classify three diagnostic indicators, so the algorithm has larger amount of calculation than one single diagnostic index. In addition, the improved D-S evidence fusion should consider the combination output of expert diagnosis, artificial neural network and MSVM to obtain more objective and accurate reliability distribution, and further improving the practicality and effectiveness of the multi-modal COVID-19 autonomous diagnosis system. The next work focuses on the optimal matching of different diagnostic indicators with low cost to improve the application effect of D-S fusion theory in COVID-19 recognition.

Declaration of competing interest

The authors declare that they have no known competing financial interests or personal relationships that could have appeared to influence the work reported in this paper.

Acknowledgments

This research has been funded by Beijing Natural Science Foundation (L192064, M21018) and Hainan Province Science and Technology Special Fund under Grant ZDYF2021GXJS205.

References

[1] Willem Joost Wiersinga, Andrew Rhodes, Allen C. Cheng, Sharon J. Peacock, Hallie C. Prescott, Pathophysiology, transmission, diagnosis, and treatment of coronavirus disease 2019 (COVID-19): A review, JAMA (2020).
[2] Catrin Sohrabi, Zaid Alsafi, Niamh Kelly O'Neill, Mehdi Khan, Ahmed Kerwan, Ahmed Al-Jabir, Christos Iosifidis, Riaz Ahmed Agha, World health organization declares global emergency: A review of the 2019 novel coronavirus (COVID-19), Int. J. Surg. (London, England) 76 (2020) 71–76.
[3] Tao Ai, Zhenlu Yang, Hongyan Hou, Chenao Zhan, Chong Chen, Wenzhi Lv, Qian Tao, Ziyong Sun, Liming Xia, Correlation of chest CT and RT-PCR testing in coronavirus disease 2019 (COVID-19) in China: A report of 1014 cases, Radiology (2020).
[4] Zheng Ye, Yun Zhang, Yi Wang, Zixia Huang, Bin Song, Chest CT manifestations of new coronavirus disease 2019 (COVID-19): A pictorial review, Eur. Radiol. 30 (2020) 4381–4389.
[5] Feng Pan, Tianhe Ye, Peng Sun, Shan Gui, Bo Liang, Lingli Li, Dandan Zheng, Jiazheng Wang, Richard L. Hesketh, Lian Yang, Chuansheng Zheng, Time course of lung changes on chest CT during recovery from 2019 novel coronavirus (COVID-19) pneumonia, Radiology (2020).
[6] Najmul Hasan, Yukun Bao, Ashadullah Shawon, Yanmei Huang, DenseNet convolutional neural networks application for predicting COVID-19 using CT image, Sn Comput. Sci. 2 (2021).
[7] Kenneth H. Dinnon, Sarah R. Leist, Alexandra Schäfer, Caitlin E. Edwards, David R. Martinez, Stephanie A. Montgomery, Ande West, Boyd L. Yount, Yixuan J. Hou, Lily E. Adams, Kendra L. Gully, Ariane J. Brown, Emily Huang, Matthew D Bryant, Ingrid C Choong, Jeffrey S. Glenn, Lisa E. Gralinski, Timothy P. Sheahan, Ralph S. Baric, A mouse-adapted model of SARS-CoV-2 to test COVID-19 countermeasures, Nature 586 (2020) 560–566.
[8] Çinare Oğuz, Mete Yaganoglu, Detection of COVID-19 using deep learning techniques and classification methods, Inf. Process. Manage. 59 (2022) 103025.
[9] Rongyao Hu, Jiangzhang Gan, Xiaofeng Zhu, Tong Liu, Xiaoshuang Shi, Multi-task multi-modality SVM for early COVID-19 diagnosis using chest CT data, Inf. Process. Manage. 59 (2021) 102782.
[10] Guowei Wang, Shuli Guo, Lina Han, Anil Baris Cekderi, Xiaowei Song, Zhilei Zhao, Asymptomatic COVID-19 CT image denoising method based on wavelet transform combined with improved PSO, Biomed. Signal Process. Control 76 (2022) 103707.
[11] Celestine Iwendi, Ali Kashif Bashir, Atharva Peshkar, R. Sujatha, Jyotir Moy Chatterjee, Swetha Pasupuleti, Rishita Mishra, Sofia K. Pillai, Ohyun Jo, COVID-19 patient health prediction using boosted random forest algorithm, Front. Public Health 8 (2020).
[12] Khaled Bayoudh, Fayçal Hamdaoui, Abdellatif Mtibaa, Hybrid-COVID: A novel hybrid 2D/3D CNN based on cross-domain adaptation approach for COVID-19 screening from chest X-ray images, Phys. Eng. Sci. Med. 43 (2020) 1415–1431.
[13] Yu-Dong Zhang, Suresh Chandra Satapathy, Shuaiqi Liu, Guang-Run Li, A five-layer deep convolutional neural network with stochastic pooling for chest CT-based COVID-19 diagnosis, Mach. Vis. Appl. 32 (2021).
[14] Mohamed Abd Elaziz, Mohammed A A Al-Qaness, Esraa Osama Abo Zaid, Songfeng Lu, Rehab Ali Ibrahim, Ahmed A Ewees, Automatic clustering method to segment COVID-19 CT images, PLoS One 16 (2021).
[15] Ophir Nave, Uziel Shemesh, Israel Hartuv, Applying Laplace adomian decomposition method (LADM) for solving a model of Covid-19, Comput. Methods Biomech. Biomed. Eng. 24 (2021) 1618–1628.

[16] Ahmed M. Anter, Diego Oliva, Anuradha D. Thakare, Zhiguo Zhang, AFCM-LSMA: New intelligent model based on Lévy slime mould algorithm and adaptive fuzzy C-means for identification of COVID-19 infection from chest X-ray images, Adv. Eng. Inform. 49 (2021) 101317.

[17] Makram Soui, Nabiollah Mansouri, Raed I. Alhamad, Marouane Kessentini, Khaled Ghédira, NSGA-II as feature selection technique and AdaBoost classifier for COVID-19 prediction using patient's symptoms, Nonlinear Dynam. 106 (2021) 1453–1475.

[18] Keli Hu, Liping Zhao, Sheng Feng, Shengdong Zhang, Q. Zhou, Xiaozhi Gao, Yanhui Guo, Colorectal polyp region extraction using saliency detection network with neutrosophic enhancement, Comput. Biol. Med. 147 (2022) 105760.

[19] Zongda Wu, Shaolong Xuan, Jian Xie, Chongze Lin, Chenglang Lu, How to ensure the confidentiality of electronic medical records on the cloud: A technical perspective, Comput. Biol. Med. 147 (2022) 105726.

[20] Jie Zhou, Xiongtao Zhang, Zhibin Jiang, Recognition of imbalanced epileptic EEG signals by a graph-based extreme learning machine, Wirel. Commun. Mob. Comput. 2021 (2021) 5871684:1–5871684:12.

[21] Wenhe Yan, Guiling Li, Zongda Wu, Senzhang Wang, Philip S. Yu, Extracting diverse-shapelets for early classification on time series, World Wide Web (2020) 1–27.

[22] Yuan Dai, Jing Wu, Yuanzhao Fan, Jin Wang, Jianwei Niu, Fei Gu, Shigen Shen, MSEva: A musculoskeletal rehabilitation evaluation system based on EMG signals, ACM Trans. Sensor Netw. (2022).

[23] Siyuan Tang, Feifei Yu, Construction and verification of retinal vessel segmentation algorithm for color fundus image under BP neural network model, J. Supercomput. 77 (2021) 3870–3884.

[24] Binjun He, Wenbin Hu, Kang Zhang, Shunda Yuan, Xiaoliang Han, Chao Su, Jiaming Zhao, Guzong Wang, Guoxiang Wang, Liuya Zhang, Image segmentation algorithm of lung cancer based on neural network model, Expert Syst. 39 (2022).

[25] A basic framework for privacy protection in personalized information retrieval, J. Organ. End User Comput. (2021).

[26] Zongda Wu, Guiling Li, Shigen Shen, Xinze Lian, Enhong Chen, Guandong Xu, Constructing dummy query sequences to protect location privacy and query privacy in location-based services, World Wide Web 24 (2020) 25–49.

[27] Yanhong Feng, Suash Deb, Gaige Wang, Amir Hossein Alavi, Monarch butterfly optimization: A comprehensive review, Expert Syst. Appl. 168 (2021) 114418.

[28] Shimin Li, Huiling Chen, Mingjing Wang, Ali Asghar Heidari, Seyed Mohammad Mirjalili, Slime mould algorithm: A new method for stochastic optimization, Future Gener. Comput. Syst. 111 (2020) 300–323.

[29] Gaige Wang, Moth search algorithm: A bio-inspired metaheuristic algorithm for global optimization problems, Memetic Comput. 10 (2018) 151–164.

[30] Yutao Yang, Huiling Chen, Ali Asghar Heidari, Amir Hossein Gandomi, Hunger games search: Visions, conception, implementation, deep analysis, perspectives, and towards performance shifts, Expert Syst. Appl. 177 (2021) 114864.

[31] Iman Ahmadianfar, Ali Asghar Heidari, Amir Hossein Gandomi, Xuefeng Chu, Huiling Chen, RUN beyond the metaphor: An efficient optimization algorithm based on Runge Kutta method, Expert Syst. Appl. 181 (2021) 115079.

[32] Essam H. Houssein, Nabil Neggaz, Mosa E. Hosney, Waleed M. Mohamed, M. Hassaballah, Enhanced Harris Hawks optimization with genetic operators for selection chemical descriptors and compounds activities, Neural Comput. Appl. 33 (2021) 13601–13618.

[33] Ophir Gozes, Maayan Frid-Adar, Hayit Greenspan, Patrick D. Browning, Huangqi Zhang, W.-B. Ji, Adam Bernheim, Eliot Siegel, Rapid AI development cycle for the coronavirus (COVID-19) pandemic: Initial results for automated detection & patient monitoring using deep learning CT image analysis, 2020, arXiv, arXiv:2003.05037.

[34] Kunwei Li, Yijie Fang, Wenjuan Li, Cunxue Pan, Peixin Qin, Yinghua Zhong, Xueguo Liu, Mingqian Huang, Yuting Liao, Shaolin Li, CT image visual quantitative evaluation and clinical classification of coronavirus disease (COVID-19), Eur. Radiol. 30 (2020) 4407–4416.

[35] Ahmed Talat Sahlol, Dalia Yousri, Ahmed A. Ewees, Mohammed Abdulaziz Aide Al-qaness, Robertas Damaševičius, Mohamed E. Abd Elaziz, COVID-19 image classification using deep features and fractional-order marine predators algorithm, Sci. Rep. 10 (2020).

[36] Hanane Allioui, Mazin Abed Mohammed, Narjes Benameur, Belal Al-Khateeb, Karrar Hameed Abdulkareem, Begonya Garcia-Zapirain, Robertas Damaševičius, Rytis Maskeliūnas, A multi-agent deep reinforcement learning approach for enhancement of COVID-19 CT image segmentation, J. Pers. Med. 12 (2022).

[37] Shuli Guo, Guowei Wang, Lina Han, Xiaowei Song, Wentao Yang, COVID-19 CT image denoising algorithm based on adaptive threshold and optimized weighted median filter, Biomed. Signal Process. Control 75 (2022) 103552.

[38] Yi fan Jiang, Han Chen, Murray H. Loew, Hanseok Ko, COVID-19 CT image synthesis with a conditional generative adversarial network, IEEE J. Biomed. Health Inf. 25 (2021) 441–452.

[39] Shibaprasad Sen, Soumyajit Saha, Somnath Chatterjee, Seyed Mohammad Mirjalili, Ram Sarkar, A bi-stage feature selection approach for COVID-19 prediction using chest CT images, Appl. Intell. (Dordrecht, Netherlands) 51 (2021) 8985–9000.

[40] Samy Bakheet, Ayoub Al-Hamadi, Automatic detection of COVID-19 using pruned GLCM-based texture features and LDCRF classification, Comput. Biol. Med. 137 (2021) 104781.

[41] Razi J. Al-azawi, Nadia M.G. Al-Saidi, Hamid A. Jalab, Hasan Kahtan, Rabha W. Ibrahim, Efficient classification of COVID-19 CT scans by using q-transform model for feature extraction, PeerJ Comput. Sci. 7 (2021) e553.

[42] Karen Panetta, Foram Sanghavi, Sos S. Agaian, Neel Madan, Automated detection of COVID-19 cases on radiographs using shape-dependent Fibonacci-p patterns, IEEE J. Biomed. Health Inf. 25 (2021) 1852–1863.

[43] Qian Fan, Zhenjian Chen, Zhao Li, Zhanghua Xia, Jiayong Yu, Dongzheng Wang, A new improved whale optimization algorithm with joint search mechanisms for high-dimensional global optimization problems, Eng. Comput. (2021) 1–28.

[44] Minshui Huang, Xihao Cheng, Yongzhi Lei, Structural damage identification based on substructure method and improved whale optimization algorithm, J. Civ. Struct. Health Monit. (2021) 1–30.

[45] Hekmat Mohammadzadeh, Farhad Soleimanian Gharehchopogh, A novel hybrid whale optimization algorithm with flower pollination algorithm for feature selection: Case study email spam detection, Comput. Intell. 37 (2021) 176–209.

[46] Sanjoy Chakraborty, Apu Kumar Saha, Sushmita Sharma, Seyed Mohammad Mirjalili, Ratul Chakraborty, A novel enhanced whale optimization algorithm for global optimization, Comput. Ind. Eng. 153 (2021) 107086.

[47] Monika Drewnik, Zbigniew Pasternak-Winiarski, SVM kernel configuration and optimization for the handwritten digit recognition, in: CISIM, 2017.

[48] Yue Pan, Limao Zhang, Zhiwu Li, Lieyun Ding, Improved fuzzy Bayesian network-based risk analysis with interval-valued fuzzy sets and D–S evidence theory, IEEE Trans. Fuzzy Syst. 28 (2020) 2063–2077.

[49] Fuyuan Xiao, A new divergence measure for belief functions in D-S evidence theory for multisensor data fusion, Inform. Sci. 514 (2020) 462–483.

[50] Jixiang Zhao, Shanwei Liu, Jianhua Wan, Muhammad Yasir, Huayu Li, Change detection method of high resolution remote sensing image based on D-S evidence theory feature fusion, IEEE Access 9 (2021) 4673–4687.

[51] Muhammad Attique Khan, Nazar Hussain, Abdul Majid, Majed Alhaisoni, Syed Ahmad Chan Bukhari, Seifedine Kadry, Yunyoung Nam, Yudong Zhang, Classification of positive COVID-19 CT scans using deep learning, Cmc-Comput. Mater. Continua 66 (2021) 2923–2938.

[52] Changjian Zhou, Jia Song, Sihan Zhou, Zhiyao Zhang, Jinge Xing, COVID-19 detection based on image regrouping and resnet-SVM using chest X-Ray images, IEEE Access 9 (2021) 81902–81912.

[53] Young-Sang Kwak, Seo Won Song, Seong-Hee Yeo, Min Soo Kang, A study on self-diagnosis method to prevent the spread of COVID-19 based on SVM, Turk. J. Comput. Math. Educ. (TURCOMAT) (2021).

[54] M. Sahaya Sheela, Chintamani Atish Arun, Hybrid PSO–SVM algorithm for Covid-19 screening and quantification, Int. J. Inf. Technol. 14 (2022) 2049–2056.

[55] Amalendu Si, Sujit Das, Samarjit Kar, Picture fuzzy set-based decision-making approach using Dempster–Shafer theory of evidence and grey relation analysis and its application in COVID-19 medicine selection, Soft Comput. (2021) 1–15.